A phase coherence approach to identifying co-located earthquakes and tremor

J.C. Hawthorne[1] and J.-P. Ampuero[2]

[1]*Institute of Geophysics and Tectonics, School of Earth and Environment, University of Leeds, Leeds, United Kingdom. E-mail: jhawthorne@gmail.com*
[2]*Seismological Laboratory, Division of Geological and Planetary Sciences, California Institute of Technology, Pasadena, CA, USA*

SUMMARY

We present and use a phase coherence approach to identify seismic signals that have similar path effects but different source time functions: co-located earthquakes and tremor. The method used is a phase coherence-based implementation of empirical matched field processing, modified to suit tremor analysis. It works by comparing the frequency-domain phases of waveforms generated by two sources recorded at multiple stations. We first cross-correlate the records of the two sources at a single station. If the sources are co-located, this cross-correlation eliminates the phases of the Green's function. It leaves the relative phases of the source time functions, which should be the same across all stations so long as the spatial extent of the sources are small compared with the seismic wavelength. We therefore search for cross-correlation phases that are consistent across stations as an indication of co-located sources. We also introduce a method to obtain relative locations between the two sources, based on back-projection of interstation phase coherence. We apply this technique to analyse two tremor-like signals that are thought to be composed of a number of earthquakes. First, we analyse a 20 s long seismic precursor to a *M* 3.9 earthquake in central Alaska. The analysis locates the precursor to within 2 km of the mainshock, and it identifies several bursts of energy—potentially foreshocks or groups of foreshocks—within the precursor. Second, we examine several minutes of volcanic tremor prior to an eruption at Redoubt Volcano. We confirm that the tremor source is located close to repeating earthquakes identified earlier in the tremor sequence. The amplitude of the tremor diminishes about 30 s before the eruption, but the phase coherence results suggest that the tremor may persist at some level through this final interval.

Key words: Fourier analysis; Earthquake source observations; Volcano seismology; Rheology and friction of fault zones.

1 INTRODUCTION

Individual small earthquakes last just a fraction of a second. They generate seismograms with impulsive arrivals that are routinely identified and analysed. However, sometimes earthquakes occur in dense clusters, and their waveforms overlap to form tremor-like seismograms (e.g. Shelly *et al.* 2007; Gomberg *et al.* 2016). These complex seismograms, resulting from long-lasting source time functions, are difficult to identify and analyse because there may be no sharp arrivals. Further, matched filter techniques for earthquake detection are often hampered by complicated waveforms introduced by the complex source time functions. Here we analyse long-duration, tremor-like sources with a method based on frequency-domain phase coherence. The approach is similar to relative source time function analysis and empirical matched field processing (e.g. Bucker 1976; Mueller 1985; Baggeroer *et al.* 1988; Mori & Frankel 1990; Krolik 1992; Baggeroer *et al.* 1993;

Velasco *et al.* 1994; Fialkowski *et al.* 2000; Harris & Kvaerna 2010; Wang *et al.* 2015). It identifies phase coherence between sources and between stations, and can thereby identify co-located point sources even if they have arbitrarily complex source time functions.

Our phase coherence method builds on conventional matched filter techniques designed to identify two similar signals. Matched filter techniques are often used to search for similar earthquakes within a seismogram, either to relocate the events or to detect small earthquakes (e.g. Nadeau & McEvilly 1999; Gibbons & Ringdal 2009; Peng & Zhao 2009; Waldhauser & Schaff 2008). Cross-correlation methods are also used to identify small low frequency earthquakes that occur repeatedly within tremor (Ide *et al.* 2007; Shelly *et al.* 2007; Brown *et al.* 2009; Bostock *et al.* 2012). However, matched filter approaches are somewhat restricted by their search for similar waveforms. For two sources to generate similar waveforms, they must have both similar Green's functions and similar source time functions.
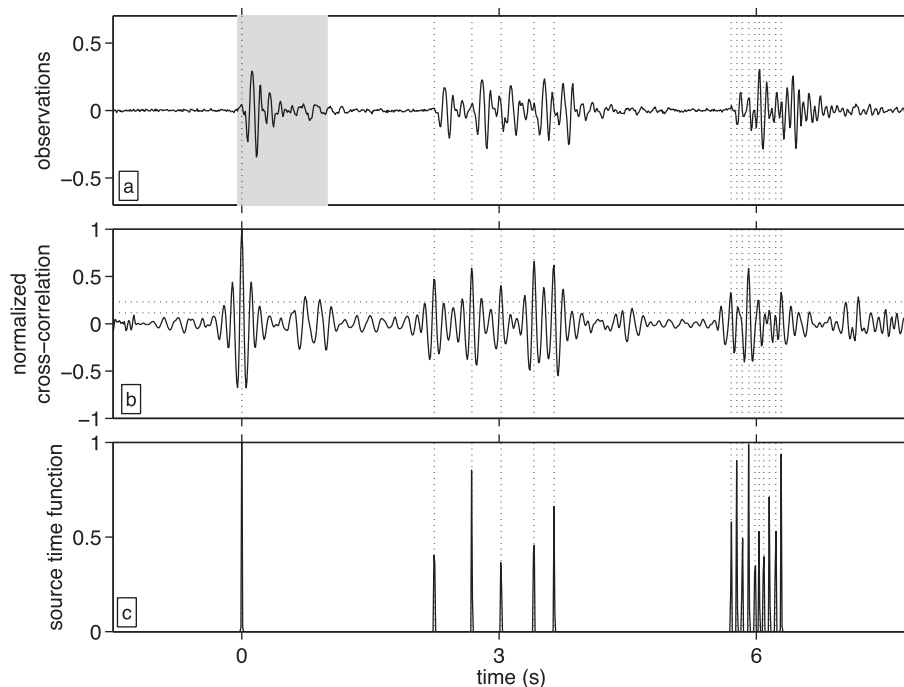
Figure 1. (a) Synthetic observations of a series of earthquakes: the convolution of a source time function (panel c) with a synthetic Green's function (seconds 0–2 in panel a). The grey bar indicates the portion of the signal we use as a template. (b) The normalized cross-correlation of the template with the observations. The cross-correlation clearly identifies the single earthquake at time 0 s, as well as the five earthquakes at time 3 s, separated by about 0.3 s. However, the cross-correlation values are smaller and more difficult to interpret near time 6 s, when 10 earthquakes separated by about 0.06 s occur. The horizontal dashed lines indicate one and two times the standard deviation expected for the cross-correlation of white noise. Vertical dashed lines in all panels indicate the times of impulsive synthetic sources. Source amplitudes are shown in panel (c).

The source time functions of tremor are often complex and variable, as there appear to be many closely spaced earthquakes (e.g. Shelly *et al.* 2007; Brown *et al.* 2009; Armbruster *et al.* 2014; Sweet *et al.* 2014). Matched filter techniques perform poorly with complicated source time functions, as we illustrate with synthetic data in Fig. 1. We convolve a synthetic template signal (grey bar in Fig. 1a) with an extended source time function (Fig. 1c) to obtain synthetic observations (Fig. 1a). Then we cross-correlate the template with the observations. The cross-correlation values (Fig. 1b) are high at times of well-separated peaks in the source time function, but they are low and variable when the source time function becomes complicated.

Complex source time functions thus present a challenge when comparing two sources at a single station. But source complexity can be an advantage when sources are recorded at a number of stations. Gibbons & Ringdal (2009) found that while extended source time functions lead to complicated cross-correlations, the same complications are often observed across a range of stations. Some researchers even use such complex but consistent source time functions to identify tremor without a template event: by searching for waveforms that are similar at multiple stations (Rubin & Armbruster 2013; Armbruster *et al.* 2014; Peng *et al.* 2015; Savard & Bostock 2015). However, for the waveforms to be similar, the stations used must have similar Green's functions. Such similarity is usually possible only if the stations are relatively closely spaced. With tremor, we often want to identify co-located but complicated sources recorded at widely spaced stations. As one example in this study, we use an earthquake recorded at regional stations as the template to identify tremor longer than 10 s originating near the earthquake hypocentre.

One approach to identifying complex signals across widely spaced stations is matched field methods, initially developed for long-duration, limited-bandwidth signals in ocean acoustics (e.g. Bucker 1976; Baggeroer *et al.* 1988; Krolik 1992; Baggeroer *et al.* 1993), but also used in the detection and location of seismic signals (Harris & Kvaerna 2010; Cros *et al.* 2011; Corciulo *et al.* 2012; Wang *et al.* 2015). In matched field processing, one constructs template Green's functions for a location of interest, using either a physical model or previously observed signals from that location. One then examines how the frequency-domain phases of these Green's functions vary among the recording stations and compares the variation to other signals potentially coming from the location of interest. Observed signals from that location are expected to show a similar pattern of phases across the observing stations, even if the source time functions are different. One can therefore identify co-located signals by stacking the coherent energy across stations.

As described in Supporting Information Section S1, the method described here can be seen as an empirical matched field technique with a modified normalization, but we implement the analysis differently. Instead of constructing a template Green's function and comparing it directly with observed signals, we divide our analysis into two steps suggested by the two tremor processing approaches noted above: intersource cross-correlation and interstation cross-correlation. First, we cross-correlate the two sources observed at each station, as in template matching approaches (e.g. Nadeau & McEvilly 1999; Ide *et al.* 2007; Shelly *et al.* 2007; Brown *et al.* 2009; Gibbons & Ringdal 2009; Peng & Zhao 2009; Waldhauser & Schaff 2008; Bostock *et al.* 2012). If the second source has the same Green's function as the template, this

cross-correlation will eliminate the Green's functions' phases. Only the relative phases of the source time functions will remain. These relative source time function phases may be complicated, but we expect them to be the same among the observing stations, as seen in cross-station tremor processing (Rubin & Armbruster 2013; Armbruster *et al.* 2014; Peng *et al.* 2015; Savard & Bostock 2015). We can therefore determine if the two sources are co-located by examining whether the cross-correlation phases are coherent across stations. We find that this series of processing steps has an advantage over standard matched field implementations (e.g. Baggeroer *et al.* 1993; Harris & Kvaerna 2010; Wang *et al.* 2015) in that it often allows temporal resolution of the tremor source that is shorter than the duration of the template Green's function.

In Section 2, we describe this phase coherence technique further and give synthetic examples. Supporting Information Sections S1–S3 provide more information about the technique's relationship to matched field methods and details of statistical analysis and temporal resolution. In Sections 3 and 4, we present two examples of the method in real-world settings. We analyse an emergent precursor to a M 3.9 earthquake in Nenana, AK, identified by Tape *et al.* (2013) in Section 3. In particular, in Section 3.3 we introduce a method for source location based on phase coherence stacking. In Section 4, we examine tremor composed of repeating earthquakes at Redoubt Volcano, previously analysed by Hotovec *et al.* (2013). Further details of these examples are given in Supporting Information Sections S4–S6.

2 DESCRIPTION OF THE METHOD

2.1 Mathematical basis

The method described here can be seen as a modification of relative source time function analysis (e.g. Mueller 1985; Mori & Frankel 1990; Velasco *et al.* 1994) or as a special case of empirical matched field processing (e.g. Fialkowski *et al.* 2000; Harris & Kvaerna 2010; Wang *et al.* 2015). We describe our approach in the context of matched field processing in Supporting Information Section S1. But since the basis of our method is relatively simple and implemented differently than standard matched field processing, we also describe the underlying concepts here.

To illustrate the approach, let us consider two point sources, with source time functions s_1 and s_2. The sources have the same focal mechanisms and originate in the same location, in a region that is small relative to the wavelength of the seismic waves. Both sources are recorded at two stations and have the same Green's functions for those stations: g_1 and g_2. The signal generated by source j and observed at station k may then be written as

$$d_{jk}(t) = s_j(t) * g_k(t),$$ (1)

where t is time. The signals can also be written in the frequency domain, with Fourier coefficients

$$\hat{s}_j(\omega) = S_j(\omega)e^{i\phi_j(\omega)}$$ (2)

$$\hat{g}_k(\omega) = G_k(\omega)e^{i\theta_k(\omega)}$$ (3)

$$\hat{d}_{jk}(\omega) = D_{jk}(\omega)e^{i\psi_{jk}(\omega)}.$$ (4)

Here ϕ_j, θ_k and ψ_{jk} are the phases of the Fourier coefficients at frequency ω, and S_j, G_k and D_{jk} are their moduli. The convolution relationship (eq. 1) can also be written in the frequency domain:

$$\hat{d}_{jk}(\omega) = \hat{s}_j(\omega)\hat{g}_k(\omega)$$ (5)

$$D_k(\omega)e^{i\psi_k(\omega)} = S_j(\omega)G_k(\omega)e^{i\phi_j(\omega)}e^{i\theta_k(\omega)}.$$ (6)

We focus on the phases of the observed and constituent Fourier coefficients, which are related via

$$\psi_{jk}(\omega) = \phi_j(\omega) + \theta_k(\omega).$$ (7)

Eq. (7) provides a set of four equations relating the four observed phases ψ_{11}, ψ_{12}, ψ_{21} and ψ_{22} to their constituents ϕ_1, ϕ_2, θ_1 and θ_2. The relationship suggests a simple way to test whether four observed phases ψ_{jk} result from common sources and paths. We consider a linear combination of the observed phases, the phase difference

$$\psi_{\text{diff}} = (\psi_{22} - \psi_{12}) - (\psi_{21} - \psi_{11}),$$ (8)

where we have dropped the frequency indexing for readability. If the observations result from shared sources and paths, ψ_{diff} will be zero. If the four observations are unrelated, the phases are unrelated, and the difference ψ_{diff} will be random.

Fig. 2 illustrates how the phase difference ψ_{diff} tends to zero for observations resulting from co-located point sources. In the first step of the ψ_{diff} calculation (lines 1 to 2), we subtract the two phases recorded at station 1. This subtraction eliminates the common constituent of these phases: the phase of the Green's function for station 1. It leaves only the relative phases of the source time function:

$$\psi_{21} - \psi_{11} = (\phi_2 + \theta_1) - (\phi_1 + \theta_1) = \phi_2 - \phi_1.$$ (9)

We perform a similar subtraction of the phases observed at station 2, eliminating its Green's function and again recovering the relative source phases $\phi_2 - \phi_1$. We now subtract the phases between stations (lines 2 to 3) and obtain zero.

The frequency-domain phase difference ψ_{diff} can also be seen as the result of two time-domain cross-correlations. In this context, we first want to eliminate the Green's functions' phases. Such an elimination could be achieved by deconvolving two signals observed at a single station, to obtain the relative source time functions (e.g. Mueller 1985; Mori & Frankel 1990; Velasco *et al.* 1994). However, here we choose to ignore the signals' amplitudes because amplitudes can vary strongly among the stations if there is large noise, and a few spurious large measurements could introduce large error. The relative source time functions' phases are constrained to a finite range, so by using only the phases we reduce the method's sensitivity to outliers. We obtain the relative source time functions' phases by cross-correlating the two signals at each station k, computing $x_k = d_{2k} \cdot d_{1k}$, which has Fourier coefficients

$$\hat{x}_k = \hat{d}_{1k}^* \hat{d}_{2k} = \hat{s}_1^* \hat{s}_2 |g_k|^2 = S_1 S_2 G_k^2 e^{i(\phi_2 - \phi_1)}.$$ (10)

Next, we cross-correlate between stations, computing $x_2 \cdot x_1$, to eliminate the phases of the source time functions. If the observations resulted from common sources and Green's functions, the final interstation phase should be zero, and $\hat{x}_1^* \hat{x}_2$ should be real and positive.

We can also formulate the final phase testing with a phase coherence computation. As before, we cross-correlate the observations at each station, calculating x_1 and x_2. We expect that these cross-correlations will eliminate the phases of the Green's functions, so that $\hat{x}_1$ and $\hat{x}_2$ will have the same phase, the relative phase of the source time functions. We measure the similarity in phase using the phase coherence:

$$C_p = \text{Re}\left[\frac{\hat{x}_1^* \hat{x}_2}{|\hat{x}_1^* \hat{x}_2|}\right]$$ (11)

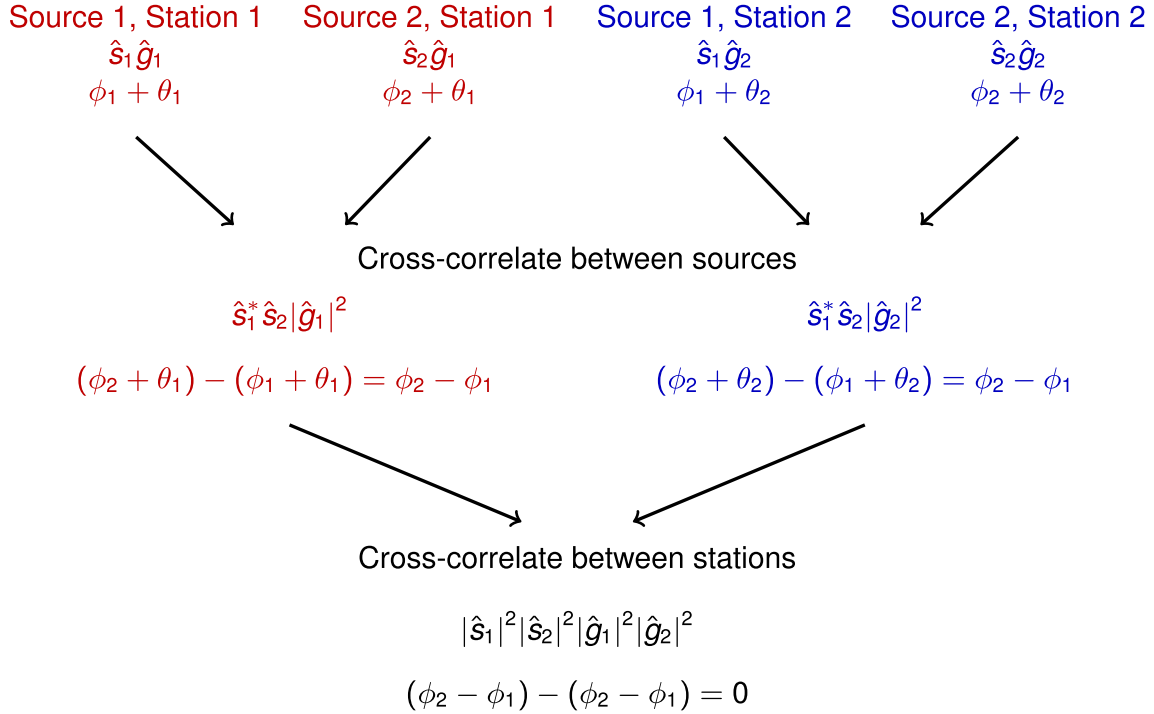| Source 1, Station 1	Source 2, Station 1	Source 1, Station 2	Source 2, Station 2
$\hat{s}_1 \hat{g}_1$	$\hat{s}_2 \hat{g}_1$	$\hat{s}_1 \hat{g}_2$	$\hat{s}_2 \hat{g}_2$
$\phi_1 + \theta_1$	$\phi_2 + \theta_1$	$\phi_1 + \theta_2$	$\phi_2 + \theta_2$

Cross-correlate between sources

$\hat{s}_1^* \hat{s}_2 |\hat{g}_1|^2$ $\hat{s}_1^* \hat{s}_2 |\hat{g}_2|^2$

$(\phi_2 + \theta_1) - (\phi_1 + \theta_1) = \phi_2 - \phi_1$ $(\phi_2 + \theta_2) - (\phi_1 + \theta_2) = \phi_2 - \phi_1$

Cross-correlate between stations

$|\hat{s}_1|^2 |\hat{s}_2|^2 |\hat{g}_1|^2 |\hat{g}_2|^2$

$(\phi_2 - \phi_1) - (\phi_2 - \phi_1) = 0$

Figure 2. Illustration of the steps to test that two signals originate in the same place. In the first line, we have hypothesized four observations: two sources each observed at the same two stations. Each observation is the convolution of a source term s_j and a path term g_k. The phases of the observed Fourier coefficients are then sums of the phases of the source time functions ϕ_j and the phases of the Green's functions θ_k. To test this hypothesis, we cross-correlate the two signals at each station (line 1 to line 2). This cross-correlation eliminates the phases θ_k of the Green's functions. We then cross-correlate the resulting cross-correlations between stations (line 2 to line 3). This second cross-correlation eliminates the phases ϕ_j of the source time functions. The Fourier coefficients produced by this cross-correlation (final line) should have zero phase. They should be real and positive.

(e.g. Bendat & Piersol 2010). If x_1 and x_2 have the same phases, both the numerator and denominator are real and positive, and C_p is 1. Large positive values of C_p—close to 1—thus indicate that the observations share common sources and paths.

The phase coherence C_p can be seen as a function of the phase difference ψ_{diff}:

$$C_p = \text{Re}\left[\frac{\hat{x}_1^* \hat{x}_2}{|\hat{x}_1^* \hat{x}_2|}\right] \tag{12}$$

$$= \text{Re}\left[\frac{\hat{d}_{11}\hat{d}_{21}^*\hat{d}_{12}^*\hat{d}_{22}}{|\hat{d}_{11}\hat{d}_{21}^*\hat{d}_{12}^*\hat{d}_{22}|}\right] \tag{13}$$

$$= \text{Re}\left[\frac{D_{11}D_{21}D_{12}D_{22}\exp\left(i\left(\psi_{11}-\psi_{21}-\psi_{12}+\psi_{22}\right)\right)}{D_{11}D_{21}D_{12}D_{22}}\right] \tag{14}$$

$$= \cos(\psi_{\text{diff}}). \tag{15}$$

Eqs (11) and (12) also suggest an alternative way to calculate C_p that is more efficient, especially for large numbers of stations. If $\hat{x}_1$ and $\hat{x}_2$ have the same phase, the sum $\hat{x}_1/|\hat{x}_1| + \hat{x}_2/|\hat{x}_2|$ will also have that phase, and it will have amplitude 2. If $\hat{x}_1$ and $\hat{x}_2$ have different phases, the sum will have smaller amplitude. In Supporting Information Section S2.3.2 (Supporting Information eq. S17), we note that C_p can be written as a function of the *phase* walkout $s = |\sum \hat{x}_k/|\hat{x}_k||$, which is summed over stations k. The phase walkout is a common statistic in the analysis of tidal triggering (e.g. Schuster 1897; Rydelek & Hass 1994; Tanaka *et al.* 2002). We use statistics from phase walkout analysis to better formulate significance tests for C_p in Supporting Information Section S2. Writing C_p in terms of the phase walkout summation also better reveals the equivalence between our processing and empirical matched field analysis (see Supporting Information

Section S1). The phase walkout is similar to an energy-based detection statistic commonly used in matched field processing (e.g. Bucker 1976; Baggeroer *et al.* 1993; Harris & Kvaerna 2010; Wang *et al.* 2015), though the phase walkout uses a different normalization and weighting of the contributing vectors $\hat{x}_k$.

Often we want to compute our detection statistic C_p and the phase difference ψ_{diff} as averaged over some frequency range. We define the broad-band coherence as the complex number

$$C = \frac{1}{\sum_{m=1}^{m=N} w_m}\sum_{m=1}^{m=N} w_m \left[\frac{\hat{x}_{1m}^* \hat{x}_{2m}}{|\hat{x}_{1m}^* \hat{x}_{2m}|}\right]. \tag{16}$$

Unless otherwise noted, the weightings w_m are 1 in the centre of the frequency interval and tapered to zero at its edges. If we are considering frequencies between f_1 and f_2 with a frequency resolution of df (see Section 2.2.2), $w_m = 1$ for frequencies between $f_1 + 3df$ and $f_2 - 3df$, and follows a cosine taper to zero at $f_1 - 3df$ and $f_2 + 3df$.

We compute the frequency-averaged phase coherence as

$$C_p = \text{Re}(C) \tag{17}$$

and the frequency-averaged phase difference ψ_{diff} as

$$e^{i\psi_{\text{diff}}} = \frac{C}{|C|} \tag{18}$$

so that

$$\cos(\psi_{\text{diff}}) = \frac{C_p}{|C|}. \tag{19}$$

When the observations result from the same sources and Green's functions, the phase coherence C_p is near 1, and the phase difference ψ_{diff} is near 0. When the sources or Green's functions vary among
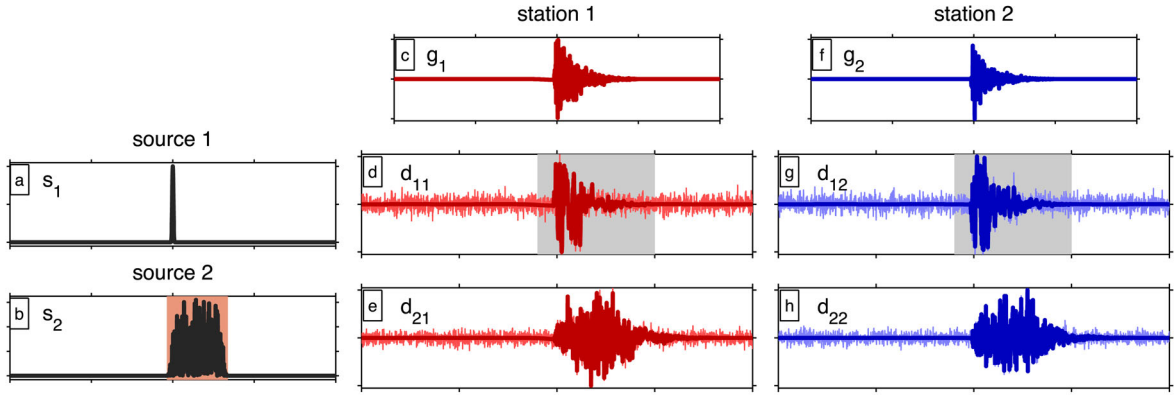
Figure 3. Synthetically generated observations. (a) The first source time function, designed to be similar to a simple earthquake. (b) The second source time function, designed to mimic tremor or a cluster of earthquakes. (c,f) The Green's functions used for each station. Station 1 is in red, and station 2 is in blue. (d,e,g,h) The synthetic observations. The darker colours are direct observations, while the lighter observations include added noise. Grey bars in panels (d) and (g) indicate the portions of the synthetic earthquake observations that we use as a template in the phase coherence computations.

the observations, the phase coherence C_p is near zero, and the phase difference ψ_{diff} is random.

2.2 Synthetic tests and practical details

To introduce the practical details of the phase coherence method and demonstrate its effectiveness, we generate and analyse synthetic data, shown in Fig. 3. The two Green's functions, g_1 and g_2, are 6 s of white noise, tapered by an exponential decay and smoothed. The first synthetic source time function s_1 simulates a small earthquake. It is a Gaussian with half-width 0.01 s. The second synthetic source time function s_2 simulates tremor. It is 5 s of the absolute value of white noise, with amplitude tapered in the first and last seconds. The four synthetic observations d_{jk} are the convolutions of the source time functions and the Green's functions.

We use the phase coherence approach described in Section 2.1 to verify that the observations share their Green's functions. We first consider the complete synthetic observations (Section 2.2.1). We then introduce windowing constraints (Section 2.2.2) and noise (Section 2.2.3).

2.2.1 Noise-free analysis

As illustrated in Fig. 2, we first cross-correlate the two observations at each station. The cross-correlations $x_k = d_{2k} \cdot d_{1k}$ are plotted in Fig. 4(a), and their phases are shown in Fig. 4(b). This intersource correlation is expected to eliminate the phases of the Green's functions, leaving the relative phases of the source time functions. Indeed, the phases of the cross-correlations are identical at the two stations, and their difference ψ_{diff} from eq. (18) is zero (Fig. 4c). The phase coherence C_p between the cross-correlations (eq. 17) is 1 (Fig. 4d). This perfect phase coherence confirms that the four synthetic observations were generated by two co-located sources.

2.2.2 Windowed analysis

The full observed time-series is rarely available in real-world analysis. We often need to truncate the records to isolate individual arrivals or to avoid intervals with low signal-to-noise ratios. To achieve this windowing, we first extract a portion of the earthquake signal. We use a 6 s window starting 1 second before the earthquake (grey bars in Fig. 3). We taper the first and last seconds with

two halves of a Blackman taper (Harris 1978). Then we proceed through the first cross-correlation as before, cross-correlating the tapered observations of the earthquake with the full tremor observations at each station (Fig. 4e).

We now wish to compute the phases of these cross-correlations within a specified time window: the 5 s bounded by a grey bar in Fig. 4(e). We window with a multitaper approach (e.g. Thomson, 1982), using 3 time-limited Slepian tapers. The tapers' energy is concentrated below 0.4 Hz, which results in a smoothing of the phase coherence spectrum for frequency spacings smaller than 0.8 Hz. We wish to sample independent phase coherence values, so we compute the phases and phase coherence at a frequency spacing of 0.8 Hz. Fig. 4(f) shows the phases of the cross-correlations obtained after windowing with the first taper. The windowing has introduced some error, so the phases are no longer identical. But the phases are still similar, suggesting that they come from a common source. Their difference is plotted in magenta in Fig. 4(h), and it is scattered around zero. The phase coherence is no longer uniformly 1, but it is still high (magenta stars in Fig. 4h).

Also plotted in Figs 4(g) and (h) are the phase differences and phase coherence values obtained with the second and third tapers (cyan and green, respectively). Averages over all three tapers are plotted in black. To average phase coherence over tapers, we first compute the taper-averaged numerator $\hat{x}_1^* \hat{x}_2$ and each of the taper-averaged amplitudes $|\hat{x}_1|^2$ and $|\hat{x}_1|^2$, weighting all tapers equally. Then we divide, computing $\hat{x}_1^* \hat{x}_2 / (|\hat{x}_1||\hat{x}_2|)$ (eq. 17). Averaging estimates with multiple tapers allows inclusion of more energy within the 5 s window, and reduced noise in the phase coherence (e.g. Thomson 1982; Percival & Walden 1993). In Supporting Information Section S2, we show that phase coherence obtained from noise can be modelled as a normal distribution with standard deviation

$$\sigma_c = 1/\sqrt{2N_f N_t}, \tag{20}$$

where N_f is the number of frequencies averaged and N_t is the number of tapers averaged. The frequency-averaged phase coherence is indicated by a horizontal black bar in Fig. 4(h). It is 0.73, more than 11 times the standard deviation expected for noise. In this average, all frequencies shown are weighted equally (all $w_m = 1$ in eq. 17).

Note that while the standard deviation $\sigma_c = 1/\sqrt{2N_f N_t}$, further increasing the number of tapers N_t would not reduce the uncertainty. Only three tapers are well concentrated within the 5 s window and at frequencies less than 0.4 Hz. In general, there are approximately
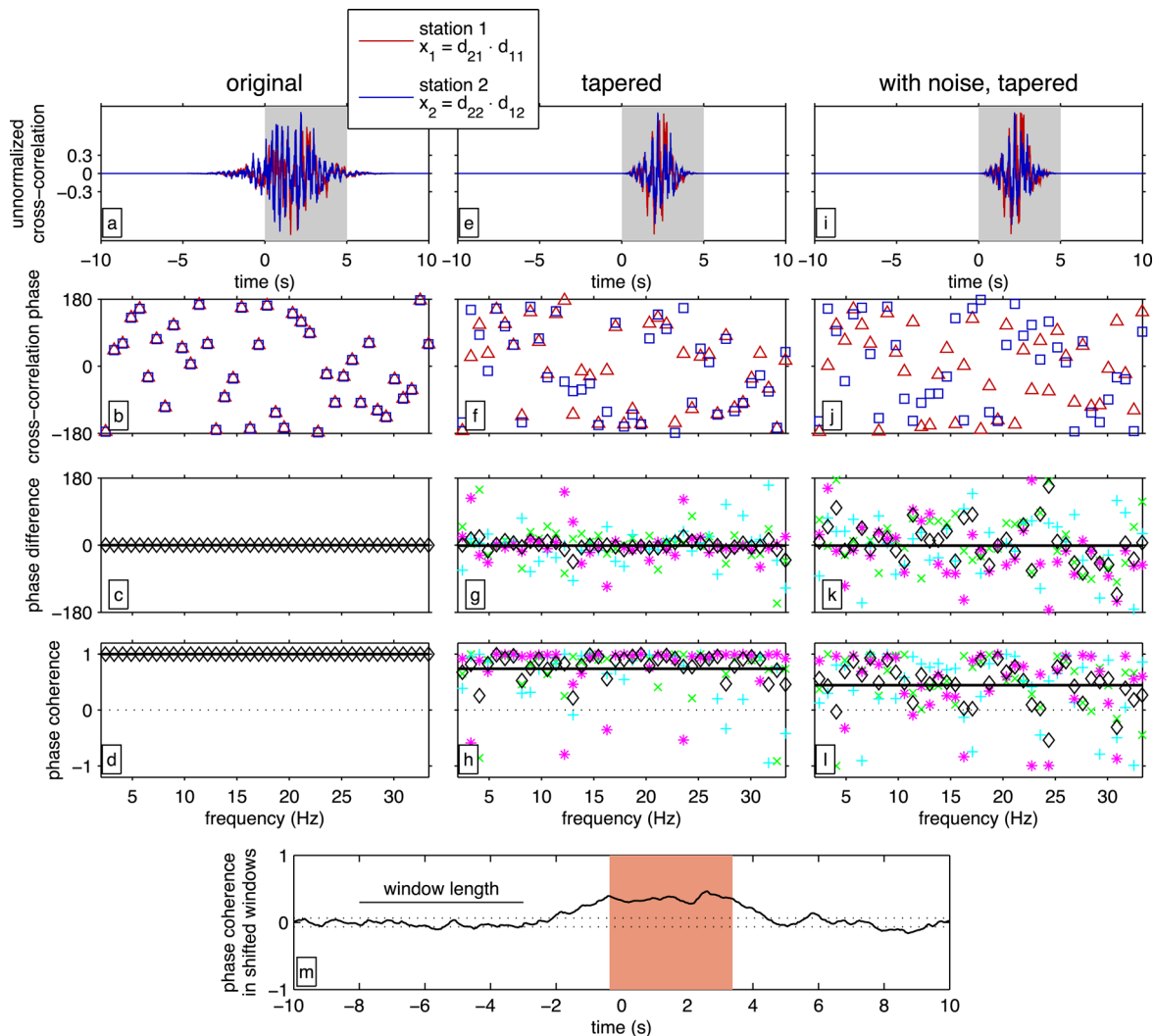
Figure 4. Results of several stages in the phase coherence analysis. (a) (Unnormalized) cross-correlations of observations of event 1 with observations of event 2. The red curve is the cross-correlation obtained at station 1, while the blue curve was obtained at station 2. (b) The phases of the cross-correlations as a function of frequency. The phases are similar between stations because the phases of the Green's functions have been eliminated. The remaining phases are the relative phases of the source time functions. (c) The difference in the phases of the cross-correlations. The difference is zero because the phases of the Green's functions were eliminated by the cross-correlations, and the phases of the source time functions were eliminated by this subtraction. The horizontal black line is an average over frequency, computed as in eq. (18). (d) Phase coherence between the two cross-correlations in panel a, computed as in eq. (17). The horizontal black line is an average over frequencies. The phase coherence is exactly 1 because the four synthetic signals being analysed share the same source time functions and Green's functions. (e) Cross-correlations, as in panel a, but here the observations of the earthquake sources were tapered before correlating, and then the cross-correlations were windowed with the most concentrated taper in the 0–5 s band (grey bar). For details, see the text. (f) The phases of the cross-correlations in panel (e). They are still similar but not identical because of the tapering. (g) The difference in the phases of the cross-correlations. As expected from panel f, the phase difference is close to but not exactly zero. The colouring in panels g and h indicates the taper used in the calculation The magenta stars are for the most concentrated taper, while the cyan crosses and green x's are for the second and third most concentrated tapers. Their average, computed as in eq. (18), is shown in black. (h) The phase coherence between the windowed cross-correlations in panel (e). The phase coherence is still high but not exactly one. (i–l) As in panels (e)–(h), but 30 per cent noise has been added to the synthetic data before processing. (m) Frequency-averaged phase coherence in a series of overlapping 5 s windows, each centred on the times on the *x*-axis. The reddish bar in panels (a) and (m) indicate the interval with signal in the second source time function. Horizontal dashed lines mark $\pm 1\sigma$.

$2wf_c$ well-concentrated tapers within a window length w and at frequencies smaller than f_c (Slepian 1976; Percival & Walden 1993). So if we tried to increase the number of tapers by a factor of 2, we would have to allow higher-frequency energy in the tapers, and thus further smooth the phase coherence spectrum. This decreased frequency resolution would reduce the number of independent frequencies N_f by a factor of 2. Using three tapers seems a reasonable compromise between smoothing and extracting energy throughout the 5 s window. In what follows, when we change the window length w from 5 s, we continue to use three tapers but change the

allowable frequency range. We use the time-limited Slepian tapers with >90 per cent of their energy at frequencies smaller than $1/w$.

For these synthetics, we consider multiple frequencies and tapers, but only one station pair. Often, however, we will wish to average the phase coherence obtained at multiple station pairs. Such an average leads to slightly more complicated statistics for our significance tests because there are more station pairs than there are stations, and thus not all of the values being averaged are independent. In Supporting Information Section S2.3 we describe the appropriate statistics for testing the significance of phase coherence averaged

Table 1. Parameters used for the phase coherence calculations to examine the Nenana precursor and Redoubt tremor. Note that some parameters are changed in searching for the preferred locations, as described in the text. The reasoning for using these parameters is given in the final column.

Parameter	Nenana	Redoubt	Reasoning
Template window since *P* arrival	−0.5 to 4.5 s	−1 to 9 s	Good signal to noise without extending too far into later phases
Taper length on each edge of template	0.5 s	1 s	Avoids spurious offsets at window limits at frequencies of a few Hz
Initial pre-extraction filtering	>0.75 Hz	>0.4 Hz	Excludes signals that cannot be resolved with the window lengths
Window length for phase coherence	3 s	10 s	Reasonable signal and frequency resolution with temporal resolution of interest
Number of tapers	3	3	Get energy throughout the window with reasonable frequency resolution

over frequencies, tapers, and station pairs. The phase coherence distributions of noise are nearly normal distributions when we focus on values smaller than the standard deviation, which is found to be $\sigma_c = 1/\sqrt{2N_f N_t N_p}$, with N_p the number of station pairs. Farther from the origin, the phase coherence distributions are biased toward positive values. We give an analytical estimate of the expected distribution in Supporting Information eq. (S19), but in this study we numerically compute the random distributions of phase coherence for null hypothesis testing, as described in Supporting Information Section S2.3.1.

2.2.3 Synthetics with noise

Uncertainties in the phase coherence become especially useful as we consider noisy observations. To mimic observational noise in our synthetic observations, we add white noise to each of the 'observed' waveforms in Fig. 3. The standard deviation of the noise is 0.3 times the standard deviation of the synthetic signal in the 0 to 3 s interval. These noisy signals are plotted in lighter colours in Fig. 3.

We process the noisy signals as described in Section 2.2.2, with the same windowing. The results are plotted in Figs 4(i)–(l). As before, the phase differences are scattered around zero (Fig. 4k). The frequency-averaged phase coherence (Fig. 4l) is 0.48, more than seven times the expected standard deviation. The phase coherence approach thus verifies the origin of the synthetic signals despite the noise.

We also compute the phase coherence in intervals dominated by noise, before and after the coherent synthetic signal. Fig. 4(m) shows the frequency-averaged phase coherence through time, in a series of overlapping windows. The phase coherence is high in windows that include part of the tremor-like source time function (reddish bars in Figs 4b and m). Note that the duration of high phase coherence is not significantly smeared through time, even though the Green's functions used are 6 s long. In Supporting Information Section S3, we show that the temporal smearing of coherence is determined not by the duration of the Green's functions, but by the duration of the Green's functions' autocorrelations, which are usually much shorter than the Green's functions themselves. Computing the phase coherence with the steps here—with the intersource cross-correlation followed by the interstation phase coherence—thus usually allows for better time resolution than one could obtain by directly comparing the template Green's function with an interval at least as long as the template, as is standard in matched field processing (e.g. Baggeroer *et al.* 1993; Harris & Kvaerna 2010; Cros *et al.* 2011; Corciulo *et al.* 2012; Wang *et al.* 2015). The temporal resolution taken advantage of here is similar to that used

in Vibroseis sweeps, which input long-duration template sources but obtain short-duration cross-correlations with those templates (e.g. Lindseth 1968). The difference here is that our templates are not complicated enough that their autocorrelations are nearly delta functions, so we must examine the frequency-dependent phases in order to identify other signals with the same Green's functions.

The theory and synthetics developed here and in Supporting Information Section S2 allow us to predict high phase coherence for co-located point sources, to determine the expected timing of that high phase coherence, and to test the significance of an observed phase coherence in the presence of unrelated noise. However, our simple synthetics ignore a range of additional practical complications that may lead to decoherence. For instance, the sources could have finite spatial extent, so that different stations are sensitive to slightly different apparent source time functions. Or the sources might be near each other but not precisely co-located, so that the Green's functions are similar but not identical. In these cases, the phase coherence would be reduced. However, as long as the sources' effective Green's functions are approximately the same, we would expect preferentially positive phase coherence. Note that throughout this paper, we query the significance of the observed phase coherence values, but we do not attempt to interpret them further. We simply test the significance of the observed phase coherence relative to the null hypothesis of unrelated signals.

2.3 Summary of the method

The practical implementation of our interstation phase coherence method can be summarized as follows. The parameter values used in the real-world examples are listed in Table 1.

(i) High-pass filter all seismograms to reduce potential complications from signals with periods much longer than the window lengths.

(ii) Extract the template of interest. Taper the edges to avoid any spurious offsets at the window limits.

(iii) At each station, cross-correlate the template with the target seismograms.

(iv) Extract the cross-correlations in a window of interest, preserving the same time lag at all stations.

(v) Taper the extracted cross-correlations. Compute the Fourier coefficients of the tapered cross-correlations for each taper of interest.

(vi) Compute the phase coherence of the Fourier coefficients between pairs of stations. Average the cross-spectra and the amplitudes over tapers before doing the division to obtain the coherence.
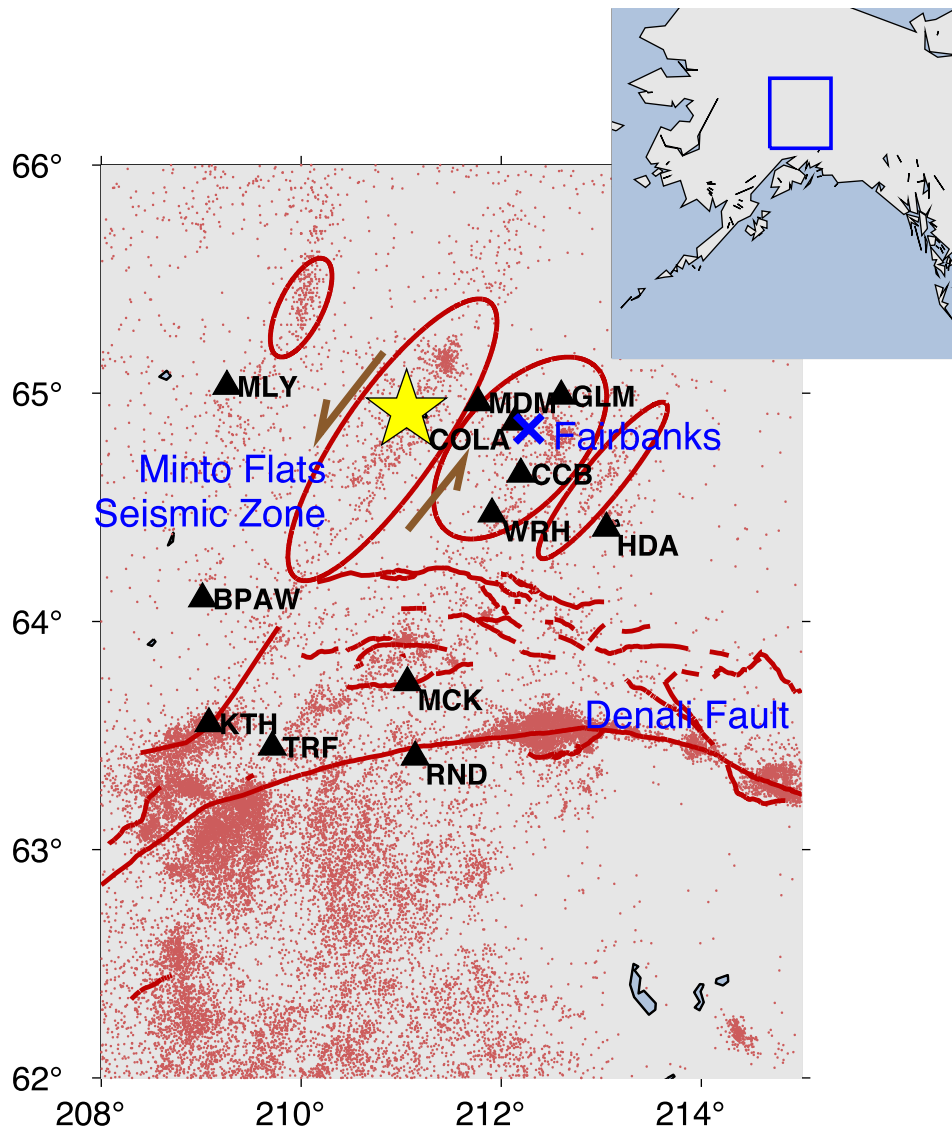
Figure 5. Location of the *M* 3.9 Nenana earthquake. The earthquake occurred at 19 km depth in the left lateral Minto Flats seismic zone in central Alaska. Dots are *M* > 2 earthquake locations from the ANSS catalogue. Triangles indicate the stations used. Red lines are quaternary faults (Koehler *et al.* 2012).

(vii) Average the phase coherence over frequencies and station pairs.

(viii) Compare the phase coherence with values expected by chance, as calculated in Supporting Information Section S2.

3 *M* 3.9 NENANA, AK PRECURSOR

3.1 Setting and background

We now wish to confirm the origin of a real signal: the emergent precursor to a *M* 3.9 earthquake near Nenana, AK, identified by Tape *et al.* (2013). The earthquake occurred on 2012 April 11 at 19 km depth in the Minto Flats seismic zone (Fig. 5) and was recorded at stations in the Alaska Regional Seismic Network. Seismograms recorded before (panel a) and after (panel b) the *P* arrivals are shown in Fig. 6. Upon initial inspection, the mainshock seismograms (panel b) show a typical earthquake with a sharp *P* arrival. However, when the records before the earthquake are displayed at an amplified scale

(panel a), they reveal an emergent signal that grows in the 20 s before the earthquake.

The signals preceding the Nenana earthquake are especially intriguing because the earthquake was likely triggered by the surface waves of the 2012 *M* 8.6 offshore Sumatra earthquake. Tape *et al.* (2013) showed that the surface waves created slip-encouraging stresses on the mainshock fault about 70 s before the earthquake. But at the time of the earthquake, the dynamic stresses discouraged slip, so Tape *et al.* (2013) hypothesized that the passing surface waves triggered a slow nucleation that eventually led to the mainshock, and that this tremor-like signal is associated with the nucleation—that accelerating aseismic slip triggered a number of small earthquakes within or around the nucleation region. If the foreshock sequence was triggered by the mainshock nucleation, the precursor may provide information about the growing aseismic slip.

The seismic signal that may reflect the nucleation process becomes observable about 25 s before the earthquake (Fig. 7c). The signal grows exponentially in amplitude up to the mainshock time (Tape *et al.* 2013). Tape *et al.* (2013) located the precursor to within
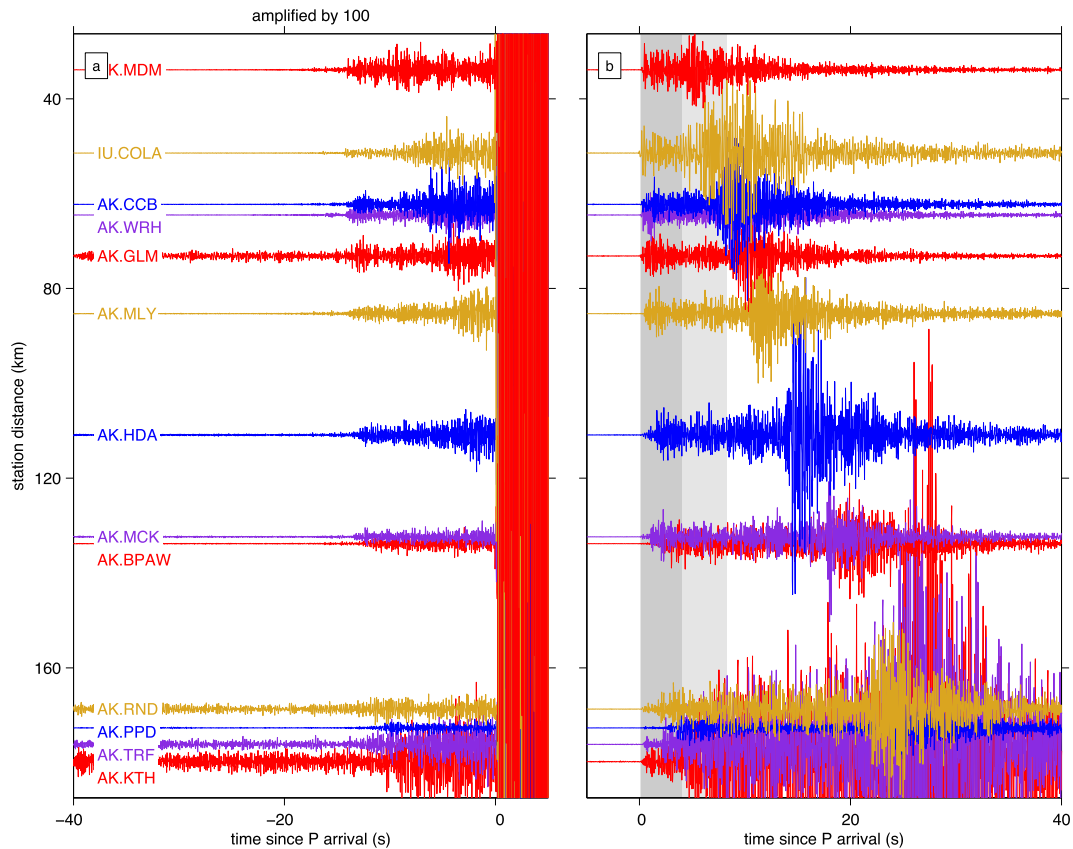
Figure 6. Seismograms just (a) before and (b) after the P arrivals from the *M* 3.9 Nenana earthquake. Seismograms are offset vertically according to the earthquake-station distance. In panel b, the seismograms of the earthquake are normalized by the maximum amplitude in the first 4 s of the *P*-wave arrival. In panel a, the amplitudes are increased by a factor of 100. The seismograms show a gradually increasing signal in the 20 s before the earthquake. The darker grey bar indicates the 4 s template window used for the phase coherence analysis. The lighter grey bar includes a 7 s window used when searching for the precursor location.

a few tens of kilometres of the earthquake using the seismograms' amplitudes. Their results were consistent with a co-located precursor and mainshock. Here we use phase coherence to reduce the location uncertainty of the precursor by one order of magnitude—to less than 2 km—and to identify variation in energy within the 25 s signal.

3.2 Precursor time history

3.2.1 Normalized cross-correlation

Before using the new phase coherence method, however, we consider a more standard approach to extracting signals from tremor: normalized cross-correlation (e.g. Shelly *et al.* 2007; Brown *et al.* 2009). The precursor is hypothesized to be composed of small earthquakes in the same location as the mainshock. Ideally we would then compare the precursor to records of small earthquakes known to be in the mainshock location. Here, however, we wish to confine our analysis to the available mainshock data, so we simply search for signals similar to the mainshock observations. We note, however, that the *M* 3.9 earthquake is not an ideal template for normalized cross-correlation analysis, as it may be complex within the 1–10 Hz frequency band of interest.

For our cross-correlations, we identify stations with low-noise recordings of the precursor (all those in Fig. 6), bandpass filter the data to 1–10 Hz, and extract 4 s after the mainshock *P* arrival, plus 0.5 s of tapered signal on each side. The 4 s template window

is chosen to use a significant fraction of the coda without including the S arrivals, and the 1–10 Hz frequency band has high a signal-to-noise ratio, multiple periods within the 4 s window, and wavelengths that can give subkilometre relative locations of similar signals—a location accuracy likely comparable to the spatial extent of the *M* 3.9 Nenana earthquake. Cross-correlations from all stations are averaged at common lags. The average cross-correlation of the mainshock template and the previous 50 s is shown in Fig. 7(d), and Fig. 8(d) shows an expansion of the −22 to −7 s interval before the mainshock origin time. The cross-correlation does reach large values—sometimes four times the standard deviation expected for white noise (described in e.g. Bendat & Piersol 2010), which is within 20 per cent of the standard deviation obtained by cross-correlating with noise in the hours before the earthquake. The high cross-correlation values during the precursor imply signals similar to the earthquake. In some cases, the cross-correlations appear to indicate relatively complex signals. For instance, at −15 s there is a group of 5 peaks spread over 1 second—perhaps a cluster of foreshocks.

3.2.2 Phase coherence calculation

If peaks in the cross-correlation represent a cluster of small foreshocks, the phase coherence should identify them as an extended but coherent source. We compute the phase coherence between the earthquake and the 50 s of data before it, following the method described in Section 2. We high-pass filter with a cut-off frequency of
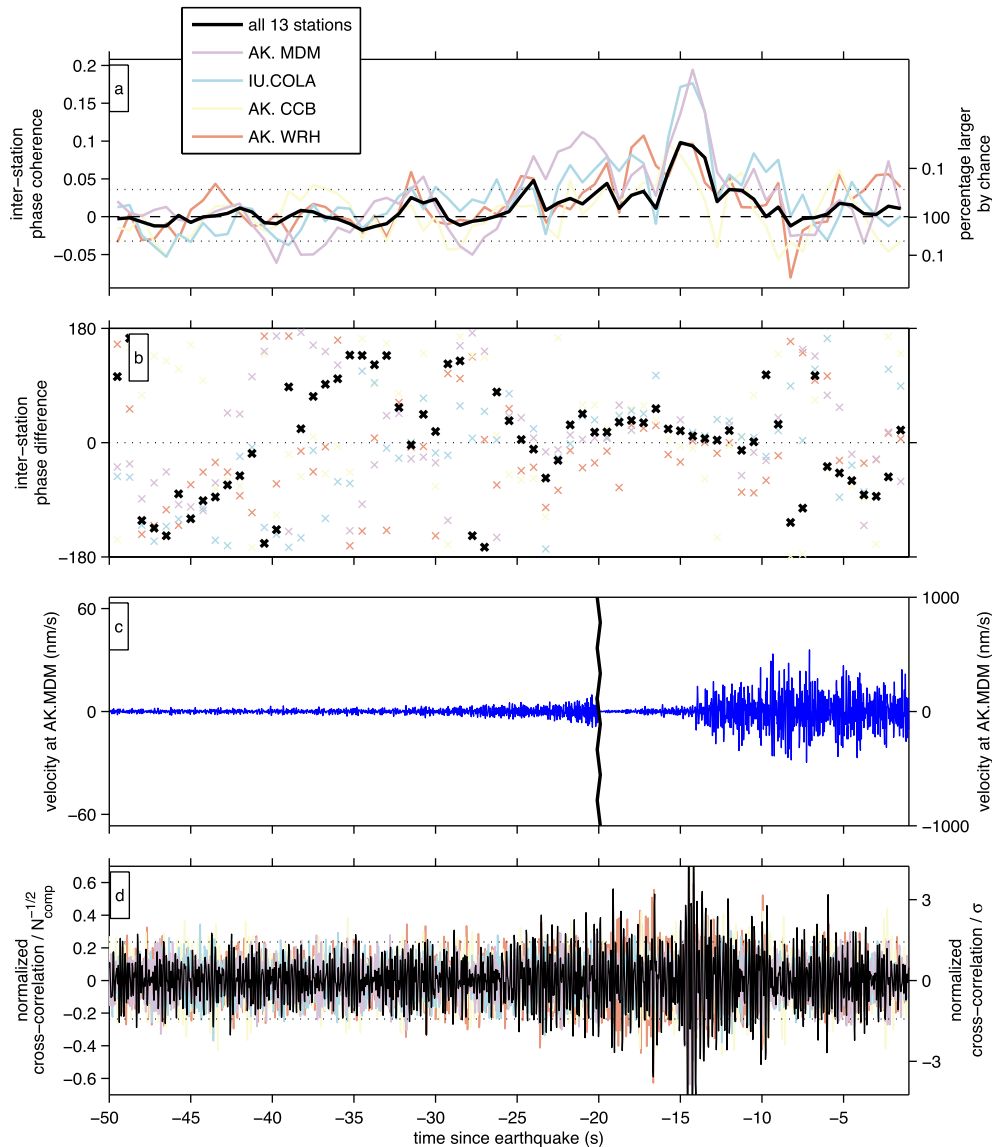
Figure 7. (d) Normalized cross-correlation between the mainshock *P*-wave signal and the precursor. Coloured curves are for individual stations, and the black curve is an average over all available stations. (a) Interstation phase coherence and (b) Interstation phase difference in the 50 s leading up to the earthquake. The black curve shows the average over all available station pairs, while the coloured curve shows the average over only pairs with the indicated station. Each coherence value is computed for a 3 s window centred at the plotted time. The right hand axis in panel a indicates the significance of the station-averaged phase coherence. The dotted lines mark the expected range of values expected with 95 per cent probability. (c) Velocity seismogram recorded at AK station MDM (the station closest to the mainshock epicentre). Note that the record is amplified by a factor of 15 more than 20 s before the mainshock, left of the black line, and that the left- and right-hand axes apply to the left and right sides of the line, respectively.

0.75 Hz to exclude long-period signals and then extract a template: 4 s after the *P* arrival, plus 0.5 s of tapered signal on each side. We cross-correlate this template with the precursor observation at each station and compute the phase differences between stations. The precursor observation is tapered to zero starting 0.5 s before the earthquake to avoid contamination from the large mainshock signal.

Figs 7(b) and 8(b) show the phase differences ψ_{diff} between the cross-correlations, averaged over all station pairs and over frequencies between 1 and 10 Hz. This average ψ_{diff} is computed as the phase of the average complex coherence, as described in eq. (18). Phase calculations are done in 3 s windows (see Section 2.2.2 for details), and values are plotted at the centre of each window. We also compute the interstation phase coherence C_p in the same windows (eq. 17) and plot them in Figs 7(a) and 8(a). Note that while

here these averages are done directly, the phase walkout discussion summarized in Supporting Information eq. (S13) provides an equivalent and potentially more efficient approach to computing station-averaged phase coherence.

3.2.3 Interpretation

At the earliest times considered—50 to 30 s before the mainshock— the phase coherence hovers around zero, and the phase difference is randomly distributed. The lack of coherence suggests that there is no resolvable signal coming from the mainshock location more than 30 s before the earthquake. About 25 s before the earthquake, the phase coherence becomes positive, and the phase difference starts to cluster around zero. We compare the phase coherence with the distribution of values that would be expected for
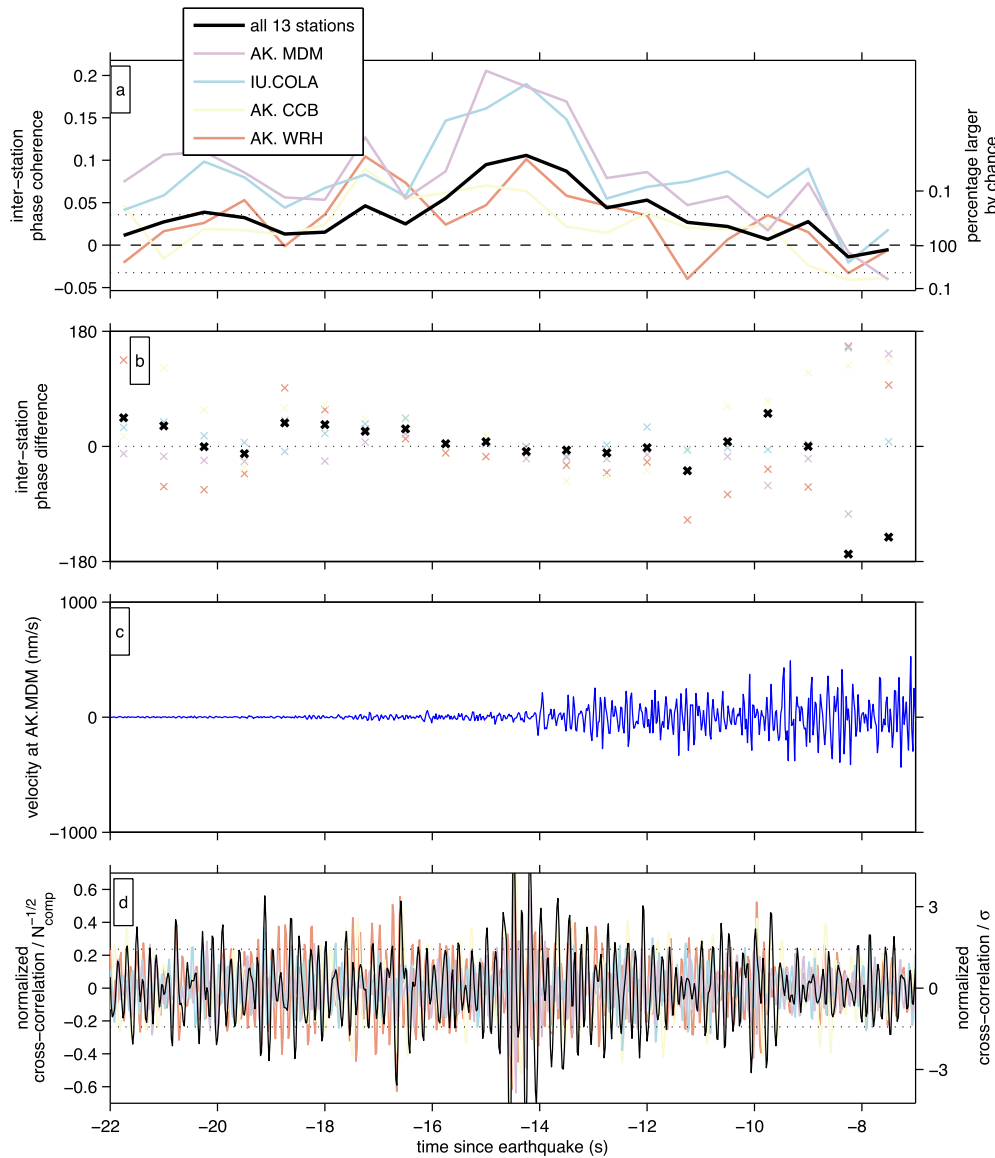
Figure 8. As in Fig. 7, but for a shorter time window: 22–7 s before the earthquake.

random noise, as calculated numerically in Supporting Information Section S2.3. The phase coherence exceeds a 99.9 per cent significance level for a few seconds but mostly stays between 0 and a 95 per cent significance level (dotted lines in Fig. 7a). Even the moderate phase coherence values obtained during the precursor are significant in that they remain positive for such a long interval: most of the 25 s remaining until the mainshock. This consistency suggests that the precursor has the same Green's functions as the mainshock.

The persistently high phase coherence also implies that the precursor generates energy over an extended period. In Supporting Information Section S3 we show that the phase coherence calculations should identify coherent energy arriving within the 3 s window used; they do not smear the phase coherence over a longer interval. The long-lasting high phase coherence of the Nenana precursor thus suggests a source that lasts at least 15 or 20 s. This duration is consistent with the seismograms, which show gradually increasing amplitudes indicative of a long-lasting source.

On the other hand, the phase coherence is not smooth during the 20 s precursor. It displays several peaks, most obviously at −15 and

−11 s. An uptick in phase coherence suggests a burst of coherent energy, perhaps individual foreshocks or clusters of foreshocks. The peak at −15 s coincides with the cluster of peaks seen in the cross-correlations. It would be consistent with a group of foreshocks occurring at that time.

However, the phase coherence measures coherence, not amplitude. The arrival at −15 s appears strong because it is larger than what came before it. The coda of such a strong signal may hide later arrivals, especially since the coda includes large signals past the 4 s included in the template. It is possible that the decreased coherence in the last 10 s before the earthquake is not the result of a decreased signal, but rather the result of a larger apparent noise from earlier arrivals, or perhaps even from other foreshocks located farther from the mainshock.

3.3 Precursor location

The high phase coherence between earthquake and precursor indicates that they have roughly the same Green's functions in the 1–10 Hz band. Such similar Green's functions imply that the two
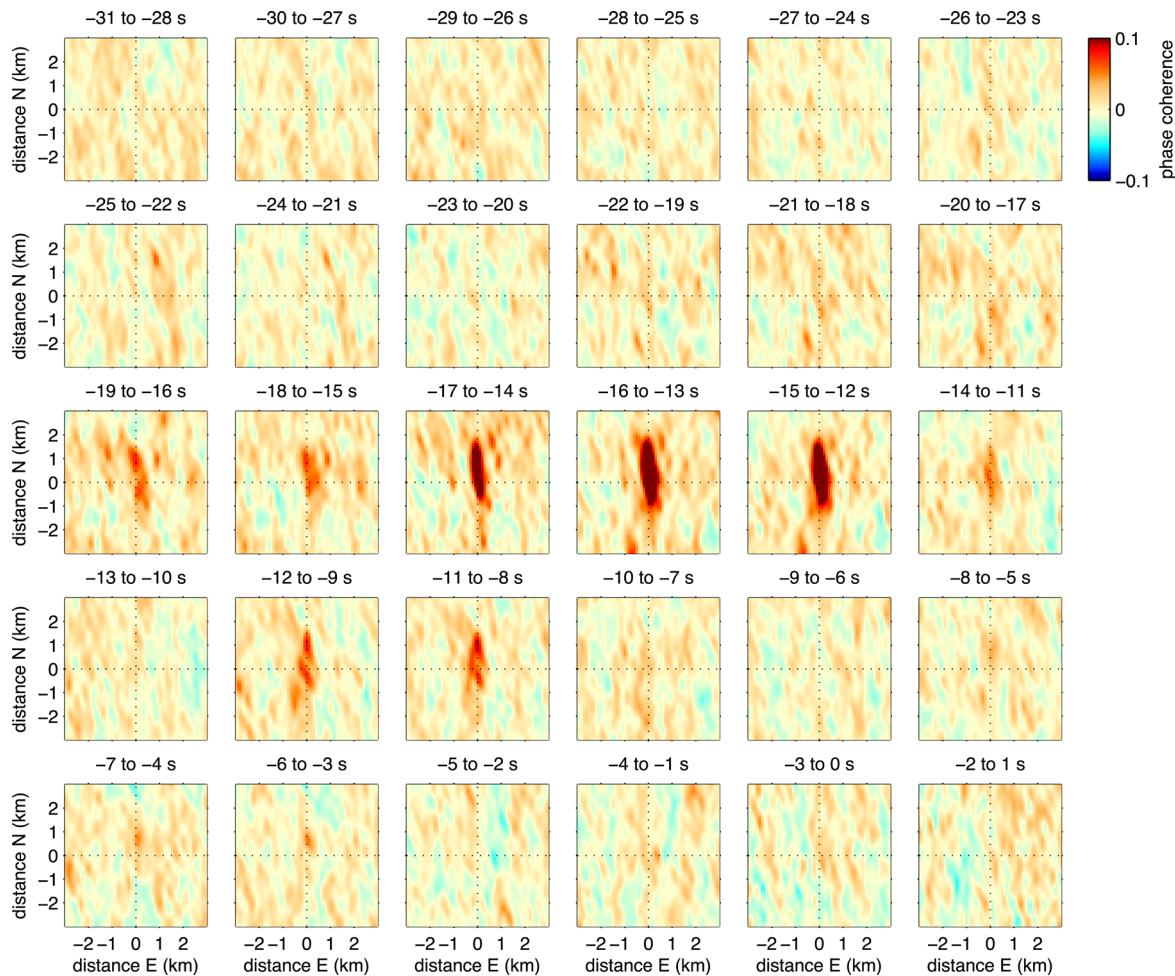
Figure 9. Phase coherence as a function of the proposed precursor location relative to the mainshock. This slice is taken with no vertical offset between the precursor and earthquake. For each location, the template seismograms are shifted according to the expected change in *P*-wave traveltime, and the phase coherence is recomputed in the 3 s windows indicated by the titles. The highest phase coherence occurs within 2 km of the mainshock. The north–south smearing arises because most of the closer stations are located east of the earthquake.

locations coincide to within the wavelengths of 1–10 Hz seismic waves, to within a few hundred metres in the propagation direction. To better determine the allowable locations, we map the phase coherence as a function of possible precursor location. The procedure is similar to back-projection source imaging (Ishii *et al.* 2007; Meng *et al.* 2011). In particular, it has similarities with matched-filter or hybrid back-projection (Yagi *et al.* 2012). However, here we introduce the use of phase coherence as the imaging field, which does not require an explicit (computed or empirical) Green's function.

We consider a grid of locations within 3 km of the earthquake. For each grid point and for the mainshock location, we compute the direct *P*-wave traveltime using TauP (Crotwell *et al.* 1999), with a 1-D velocity model similar to that used by the AEIC (Alaska Earthquake Information Center) to locate earthquakes north of 62.5°N (Beaudoin *et al.* 1992; Ratchkovski & Hansen 2002; Dixon *et al.* 2010). The seismograms are shifted by the predicted difference in traveltime between the proposed location and the mainshock location. If the precursor is in the proposed location, the improved alignment should increase the phase coherence. Note, however, that time shifts cannot correct for spatial variation in the Green's functions. If the form of the Green's functions varies strongly with location, the coherence may be low even if the time shifts are correct.

The phase coherence obtained is shown in map view and cross-section in Fig. 9 and Supporting Information Figs S7 and S8. Almost all phase coherence values larger than 0.05 (>95 per cent significance) are within 0.5 km of the earthquake in the E–W direction, and within 2 km of the earthquake in the N–S direction. The highest coherence values are about 1 km to the north. The smoothness of the image on scales shorter than 0.5 to 1 km reflects the wavelengths of the 1–10 Hz seismic waves. The coherence is smeared in the north–south direction because most of the nearby stations are located east of the earthquakes (Fig. 5). Uncertainty is larger in the vertical direction because most of the ray paths are roughly horizontal near the source. To better examine this spatial uncertainty, in Supporting Information Section S5 we calculate the phase coherence of a synthetic source as a function of relative location.

There is likely also uncertainty and decoherence associated with the finite spatial extent of the earthquake. The radius of a *M* 3.9 earthquake with a 3 MPa stress drop is around 0.5 km, comparable to that of 5–10 Hz seismic waves. Since the earthquake radiation comes from a distributed area, there is no single time shift that will allow all of the mainshock signal to be coherent with the precursory signal. The spatial distribution of source likely leads to some decoherence and a spatial smoothing of the phase coherence. The phase coherence we observe is presumably the coherence

with an average earthquake Green's function. The phase coherence map in Fig. 9 would then compare the precursor location with the earthquake centroid.

If the earthquake radius is 0.5 km and the distance from the precursor to the earthquake centroid is less than 1 km, the precursor may have occurred within the area that ruptured during the earthquake. Alternatively, it may have occurred just at the edge of the mainshock rupture. Either of these scenarios is consistent with accelerating aseismic slip triggering small foreshocks as it nucleates into the mainshock (Tape *et al.* 2013).

The location analysis also gives more confidence in the temporal changes in phase coherence identified in Section 3.2. The region of high phase coherence shows a clear spatial concentration roughly 15 and 10 s before the mainshock, at times of peaks in the phase coherence. The high phase coherence also localizes weakly near the mainshock at −23 and −6 s. These spatial peaks may suggest additional bursts of energy, which would be consistent with the precursor starting at least 25 s before the mainshock.

3.4 Discussion

The phase coherence results suggest that the precursory signal results from foreshocks occurring within 2 km of the *M* 3.9 earthquake. These closely spaced foreshocks may be driven by accelerating aseismic slip that eventually nucleates into the mainshock, as proposed by Tape *et al.* (2013). Foreshocks broadly associated with pre-seismic slip have been suggested prior to a number of earthquakes (e.g. Dodge *et al.* 1996; Richards-Dinger *et al.* 2010; Kato *et al.* 2012; Shearer 2012; Bouchon *et al.* 2013; Chen & Shearer 2013). The observation most similar to the Nenana precursor occurred before the 1999 *M* 7.6 Izmit earthquake (Bouchon *et al.* 2011). A series of repeating earthquakes occurred near the eventual hypocentre, where aseismic slip would have been accelerating into the mainshock. The repeating earthquake rate increased over about an hour as the time of the mainshock approached. The amplitude of seismic noise unassociated with identified earthquakes also increased and stayed high after the first foreshock, one day before the mainshock. That noise may have resulted from smaller foreshocks, perhaps also triggered by aseismic slip (Bouchon *et al.* 2011).

Aseismic slip prior to earthquakes is expected in models of earthquake nucleation. What varies among the models and laboratory experiments is the magnitude and timing of that slip (Dieterich 1992; Ohnaka 1992; Campillo & Ionescu 1997; Ohnaka 2000; Ampuero *et al.* 2002; Lapusta & Rice 2003; Rubin & Ampuero 2005; Ampuero & Rubin 2008; Rubinstein *et al.* 2009; Fang *et al.* 2011; Garagash & Germanovich 2012; Latour *et al.* 2013; McLaskey & Kilgore 2013; Colombelli *et al.* 2014; McLaskey & Lockner 2014). For instance, some models and observations predict that pre-seismic slip should be highly localized and release little moment (e.g. Dieterich 1992; Lapusta & Rice 2003; Rubin & Ampuero 2005; Johnston *et al.* 2006; Ampuero & Rubin 2008), while other results suggest that the width of the nucleation zone should scale with the earthquake size, and thus that the pre-seismic moment could be larger (Ohnaka 1992, 2000; Colombelli *et al.* 2014). The timing of pre-seismic slip also varies among the models. In linear slip weakening models, the moment rate increases exponentially prior to an earthquake (Campillo & Ionescu 1997; Ampuero *et al.* 2002; Ripperger *et al.* 2007). Exponential growth is also seen in some regimes of rate and state friction models (Lapusta & Rice 2003; Rubin & Ampuero 2005; Garagash & Germanovich 2012). In other

regimes of rate and station friction nucleation, on the other hand, the moment rate increases as a power law function of the time until the earthquake. The moment rate often increases roughly as time-to-failure^{-1} (Dieterich 1992; Rubin & Ampuero 2005; Ampuero & Rubin 2008; Noda *et al.* 2013b) but sometimes increases slightly slower (Ampuero & Rubin 2008; Noda *et al.* 2013b) or faster (Ampuero & Rubin 2008).

We cannot directly observe the aseismic moment rate in the Nenana precursor, but we can see that the seismic amplitude increases exponentially prior to the mainshock (Tape *et al.* 2013). In one explanation of the data, we might model this increasing amplitude as the result of an increasing number of foreshocks, with no change in the foreshocks' magnitude. If the foreshocks' amplitudes sum linearly, the seismic amplitude would be proportional to the number of foreshocks occurring. We would then model the exponentially increasing seismic amplitude as an exponential increase in the foreshock rate.

To interpret the foreshock rate in terms of an aseismic moment rate, we must make assumptions about their relationship. As one option, the foreshocks might have occurred on asperities embedded within a larger region that is slipping aseismically. Then the number of triggered events would be proportional to the moment rate. We might therefore conclude that the aseismic moment rate grew exponentially prior to the mainshock, as seen in linear slip-weakening models (Campillo & Ionescu 1997; Ampuero *et al.* 2002; Ripperger *et al.* 2007). However, we should be careful in making such a simple interpretation. In Section 3.2 we saw several peaks in the phase coherence during the precursor. The peaks indicate bursts of seismic energy, perhaps individual foreshocks or groups of foreshocks. The number of foreshocks may thus be a complicated function of the aseismic slip.

In fact, the foreshocks may occur outside the aseismic slip, perhaps at its edge (Tape *et al.* 2013). In this case, the growing seismic amplitude might reflect the number of asperities being ruptured as the nucleating region expanded. The exponentially increasing seismic amplitude might therefore imply an exponential growth of the slipping region. Such an exponential spatial growth was seen during the initial propagation of fault slip modelled with a viscous rheology (Ando *et al.* 2012) and in some laboratory experiments (Latour *et al.* 2013). In the later portions of these and other laboratory experiments, however, the slipping region was found to grow more rapidly, increasing as a power law function of time to instability (Ohnaka & Shen 1999; Latour *et al.* 2013).

As a final alternative, we should note that the Nenana precursor may not reflect aseismic slip at all. The seismic signal could result from a dense cluster of interacting foreshocks. We might imagine the precursor as a sequence of progressively larger earthquakes, each one rupturing a slightly larger area. Such a cascade model of earthquake nucleation was suggested by Ellsworth & Beroza (1995) and Beroza & Ellsworth (1996) to explain a much shorter (<1 second) but magnitude-dependent nucleation timescale. The cascade model is an appealing mechanism to explain earthquakes with size-dependent initial behaviour but little pre-seismic slip (Noda *et al.* 2013a; Colombelli *et al.* 2014; McLaskey & Lockner 2014).

The long seismic signal preceding the Nenana earthquake may be highly unusual, and perhaps related to the passing surface waves that probably triggered it. The dynamic stresses discouraged slip at the time of the mainshock and may have somehow slowed the earthquake's nucleation (Tape *et al.* 2013). Dynamically triggered earthquakes often occur minutes or hours after the seismic waves have passed. This delay is presumably facilitated by some aseismic

process like aseismic slip or fluid flow (e.g. Hill *et al.* 1993; Gomberg & Davis 1996; Hill & Prejean 2007; Brodsky & van der Elst 2010). If that process caused the emergent precursor before the Nenana earthquake, it may also cause long-duration precursors to other dynamically triggered earthquakes. Such precursors might be identified with the phase coherence technique introduced here.

4 VOLCANIC TREMOR COMPOSED OF REPEATING EARTHQUAKES

In our second demonstration of the phase coherence approach, we analyse harmonic tremor at Redoubt Volcano that is thought to be composed of repeating earthquakes (Hotovec *et al.* 2013). These repeating earthquakes occur at depths of just a few kilometres and likely result from brittle failure, perhaps on the magma conduit wall (Dmitrieva *et al.* 2013; Hotovec *et al.* 2013). Here we use the phase coherence method to confirm the relationship between the tremor and repeating earthquakes. Our analysis also suggests that tremor may have extended closer to the time of eruption than previously thought.

4.1 Background: earthquake and tremor behaviour

The tremor and earthquakes occurred before an eruption of Redoubt at 07:47 UTC on 2009 March 27. The earthquake swarm started about 10 hr prior to the eruption, and the earthquake rate gradually increased as the eruption neared (Dixon *et al.* 2010). Fig. 12(a) shows a seismogram from the last hour prior to the eruption, with more than 100 visible earthquakes. Most of the earthquakes have similar waveforms and arrival times (Buurman *et al.* 2013; Hotovec *et al.* 2013). Hotovec *et al.* (2013) therefore interpreted the earthquakes as the repeated rupture of a single patch. They interpreted the increasing earthquake rate as the result of an increasing stressing rate leading up to the eruption (Dmitrieva *et al.* 2013; Hotovec *et al.* 2013).

About 7 min before the eruption, the earthquakes began to occur so frequently that their waveforms overlap. The combined waveforms appear tremor-like, and it becomes difficult to identify individual earthquakes within the tremor. Over the next few minutes the tremor exhibited a gradually increasing frequency content. Finally, the tremor abruptly diminished about 30 s before the eruption. The smooth gradation between repeating earthquakes and tremor led Hotovec *et al.* (2013) to conclude that the tremor is composed of closely spaced repeating earthquakes. Indeed, the changing frequency content of tremor is consistent with a still-increasing earthquake rate (Hotovec *et al.* 2013). We will verify that the earthquakes and the tremor have the same Green's functions.

4.2 Earthquake templates

In order to compare the tremor with the earthquakes, we need a high-quality earthquake template. We obtain it by stacking records of 114 earthquakes in the 2 hr before the eruption (Dixon *et al.* 2010). We use data from the vertical components of 5 short-period stations operated by the Alaska Volcano Observatory (AVO): RDN, RED, NCT, DFR and RDT, shown in Fig. 10. For each earthquake, we cross-correlate 1.5 s of data after the *P* wave with data from every other event. The resulting high cross-correlations confirm that the earthquakes are similar and allow us to identify a precise relative time for each earthquake. The data are consistent with the earth-
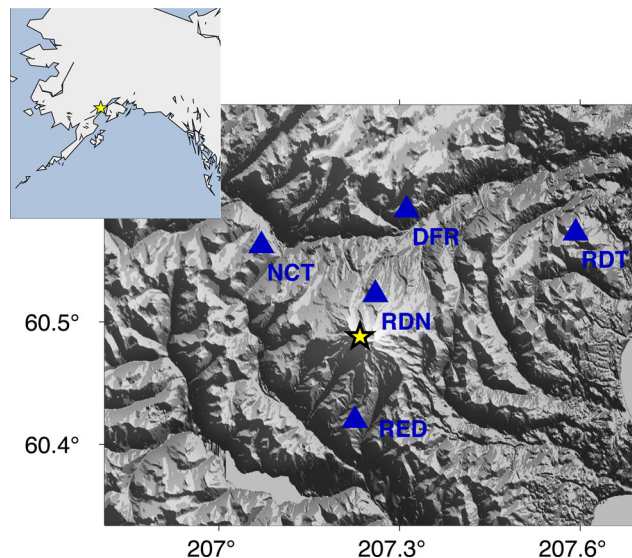

Figure 10. Shaded relief map of Redoubt Volcano and its surroundings (USGS 2015). The earthquakes and tremor are located at the star, near the summit. The AVO stations used are indicated by black triangles.

quakes being co-located, so we select only one time shift per event; no interstation time shifts are allowed.

Once the data are aligned, we check the data quality and stack the waveforms. Clipped seismograms are excluded, and each remaining seismogram is normalized by its maximum value. We stack the normalized records, weighting each seismogram by its signal-to-noise ratio—by the variance in the signal over the variance in an earlier interval. This simple weighting would result in the normalized seismogram that best fits the observed data in a least-squares sense given their noise level, assuming white noise and no interstation correlations (Tyapkin & Ursin 2005).

The stacked templates are shown in Fig. 11(a). We use the first 8 s after the *P* arrival as the templates, plus one second on either side tapered with a Blackman taper. These 8 s include both the *P* and *S* arrivals, as the stations are located within 20 km of the earthquakes. The templates have high signal to noise in the <20 Hz band, as shown in Fig. 11(b).

4.3 Phase coherence analysis

We now compute the phase coherence between the earthquake templates and the tremor. Following the approach described in Section 2, we first cross-correlate at each station, and then compute the 1–10 Hz phase coherence between the cross-correlations in 10 s windows (eq. 17). Fig. 12(b) shows the phase coherence stacked over station pairs in the hour before the eruption. Fig. 13(b) shows a shorter interval: 3 min before the eruption.

In the hour leading up to the eruption, the phase coherence shows a number of peaks associated with the repeating earthquakes. Catalogued events are indicated by dotted lines in Fig. 12. Between the clearly visible earthquakes the phase coherence is low but still positive. The significance hovers around 70 per cent, as shown on the right hand axis in Fig. 12(b). This positive background coherence likely arises because most 10 s intervals include a repeating earthquake. Hotovec *et al.* (2013) identified an earthquake every 2–5 s from 60 to 30 min before the eruption. When no earthquakes are occurring—for instance, at times several days before the eruption— the phase coherence stays near zero (grey curves in Fig. 12b).
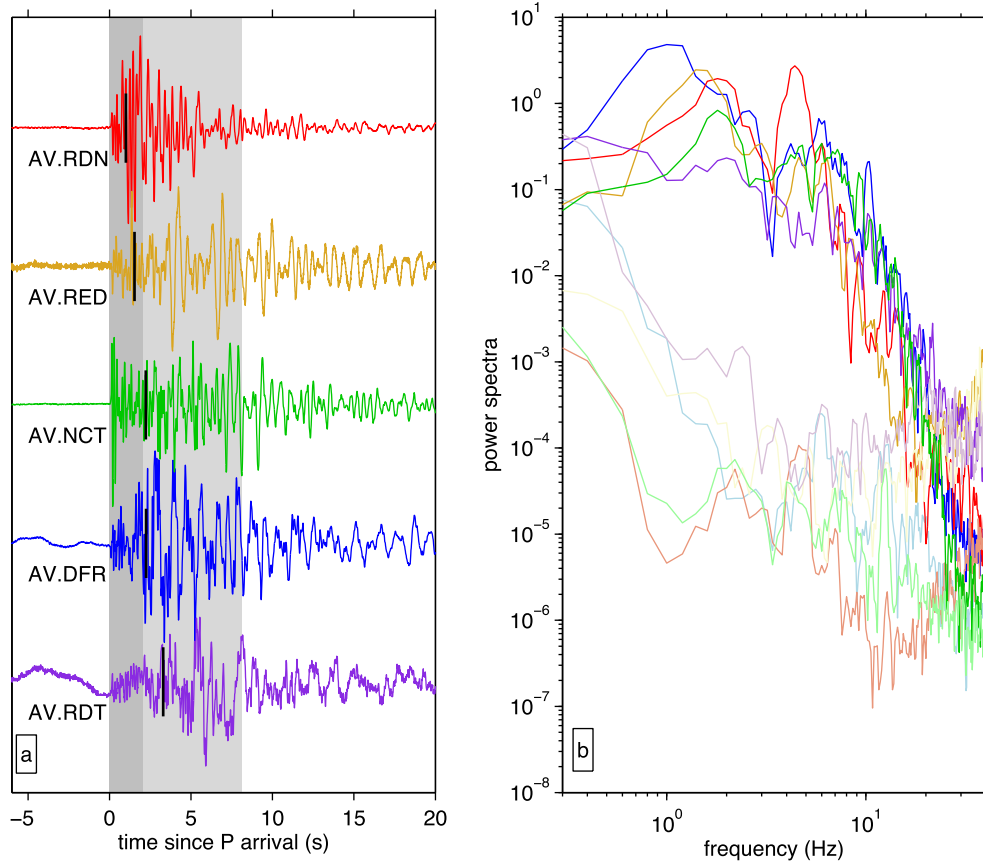
Figure 11. (a) Stacked template seismograms. The grey region from 0 to 8 s indicates the portion of the seismograms used as the template for most of the analysis. This interval includes portions of the *P* and *S* arrivals. The expected timing of the *S* arrival is indicated by the black lines. In Supporting Information Fig. S14, we redo the location calculations with a shorter, 2 s template that is dominated by the *P* arrival, delineated with the darker grey bar. (b) Darker lines: power spectra of the 8 s templates shown in panel (a). Lighter lines: power spectra of the noise in the templates, taken from the stacked signal prior to the earthquakes. Colours are as in panel (a).

The background phase coherence gradually becomes more positive in the hour before the eruption. It reaches 99 per cent significance around −10 min. At the same time, the peaks in the phase coherence diminish. This more uniform phase coherence is consistent with more closely spaced earthquakes. Now every 10 s interval includes several earthquakes that are coherent with the reference events. But no individual arrival is much stronger than those that came before, so there are no strong peaks.

The high phase coherence persists throughout the tremor, as earthquakes presumably become so frequent that their waveforms are indistinguishable. This high phase coherence is the primary result of our analysis. The high coherence implies that the tremor has the same Green's function as the earthquakes. We therefore confirm that the tremor is composed of repeating earthquakes, as Hotovec *et al.* (2013) concluded from the earthquakes' timing and locations.

About 30 s before the eruption, the tremor amplitude decreases strongly. The phase coherence during this final period also decreases, but it stays positive and significant at the 70 per cent level until after the eruption. The high phase coherence in this final interval is unlikely to result from smoothing of earlier coherent signal, as smoothing should occur only over the 10 s window we used in the phase coherence calculation (see Supporting Information Section S3). The high values may thus suggest that tremor persists over the final 30 s, just at a much reduced amplitude. However, we note that the final 20 s before the eruption include only two independent phase coherence values, each significant at the 70 per cent

level. There is a 10 per cent probability that such large values would have occurred by chance.

4.4 Tremor location

The high phase coherence between the earthquakes and the tremor suggests that they originate in nearly the same place. To determine just how close they have to be, we compute the phase coherence for a range of possible tremor locations, as in Section 3.3. The phase coherence is evaluated in 60 s long windows. The time shifts are computed using TauP (Crotwell *et al.* 1999) with a 1-D *S*-wave velocity model created for Alaskan volcanoes (Lahr *et al.* 1994; Dixon *et al.* 2010). We assume an *S*-wave velocity because the S arrival seems likely to dominate the template signal (Fig. 11). However, we obtain similar coherence maps if we use just the first 2 s of the template and assume a *P*-wave velocity model (Supporting Information Fig. S14). In the calculations shown we assume an earthquake depth of 4 km, but similar results are obtained with depths of 2, 3 or 5 km.

The phase coherence obtained during the tremor is shown in Fig. 14 and Supporting Information Figs S12 and S13. The highest phase coherence occurs within 0.5 km of the earthquakes, suggesting that the tremor and earthquakes originate within 0.5 km of each other. Since the earthquakes are mostly smaller than M2 (Dixon *et al.* 2010), and thus likely have dimensions of order 100 m,
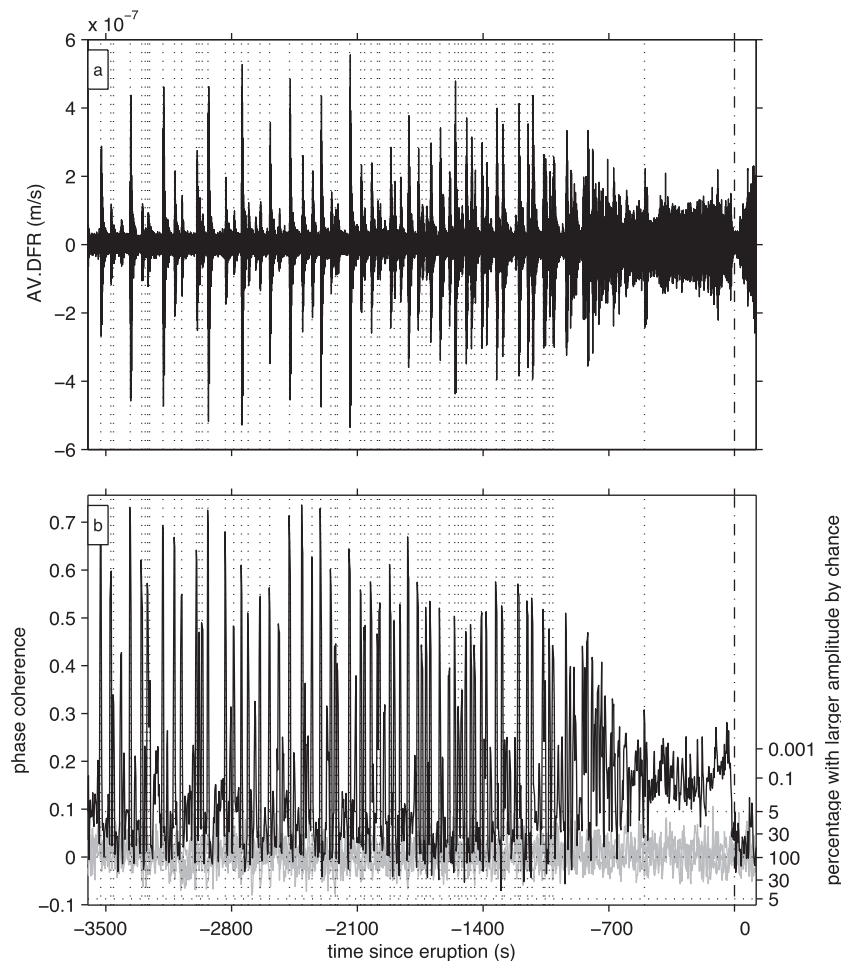
Figure 12. (a) Seismogram at one station in the 20 min before the eruption. About 100 repeating earthquakes are visible as impulsive arrivals. Vertical dotted lines indicate times of catalogued events. The earthquake rate increases in the hour prior to the eruption, and their waveforms blend into tremor about 7 min beforehand. (b) Interstation phase coherence between the repeating earthquake template and the observed signals, averaged over all station pairs. The phase coherence between the repeating earthquakes and the template is high, as expected. The phase coherence is also high during the tremor, indicating that the tremor and repeating earthquakes have the same Green's functions. Dotted lines indicate a 95 per cent significance level.

these locations would permit earthquakes and tremor that rupture the same area or adjacent areas.

4.5 Discussion

Our phase coherence results affirm Hotovec *et al.*'s (2013) conclusion that this tremor is composed of repeating earthquakes, and provide further confidence when interpreting the tremor's behaviour. For instance, Hotovec *et al.* (2013) showed that the earthquakes have focal mechanisms indicative of shear on a subvertical plane, consistent with brittle failure on the edge of a magma conduit. This brittle asperity is inferred to break more and more frequently as the stressing rate increases prior to the eruption, leading to an increasing earthquake rate and then an increasing dominant frequency in the tremor (Dmitrieva *et al.* 2013; Hotovec *et al.* 2013).

The dominant frequency continues to increase until the tremor abruptly diminishes 30 s before the eruption. Dmitrieva *et al.* (2013) proposed that the tremor stops because the fault reaches increasingly high but steady slip speeds. We observe a positive but reduced phase coherence in the final 30 s. The positive coherence suggests that the asperity continues to slip until the time of the eruption, though with lower seismic energy radiation (in the 1-10 Hz band). This continued coherence would suggest at least some variation in slip rate in the

in the last 30 s. However, we note that the final positive phase coherence values are significant only with 90 per cent probability, so they should be interpreted with caution. Despite its low significance, the positive coherence during the interval of decreasing amplitude illustrates how the method implemented here has the potential to provide independent constraints on volcanic processes.

Tremor composed of repeating earthquakes has also been observed at a variety of other volcanoes. Such volcanic tremor may be composed of stick-slip events or other impulsive sources, including rapid gas or fluid flow or the opening of fractures (e.g. Fehler 1983; Neuberg *et al.* 2000; Powell & Neuberg 2003; Iverson *et al.* 2006; Neuberg *et al.* 2006; Harrington & Brodsky 2007). Here we have shown that the phase coherence approach can be a useful tool for comparing tremor with its potential constituents. Our method is expected to work even if the impulsive source is not a stick-slip earthquake. The tremor and constituent sources simply need to have the same Green's function.

5 CONCLUSIONS

We have implemented a phase coherence method that can identify seismic sources with similar Green's functions even if the sources have very different source time functions. This technique is
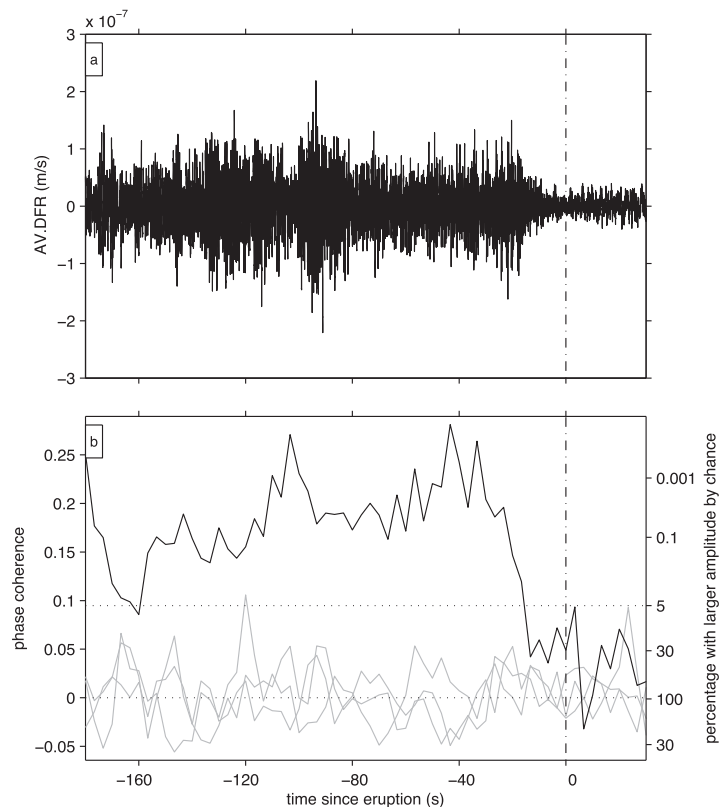
Figure 13. An expanded portion of the seismogram (panel a) and phase coherence (panel b) from Fig. 12, showing the final few minutes of tremor. The phase coherence stays high throughout the tremor. It decreases about 30 s before the eruption, when the seismogram amplitude decreases, but does not reach 0 until after the eruption.
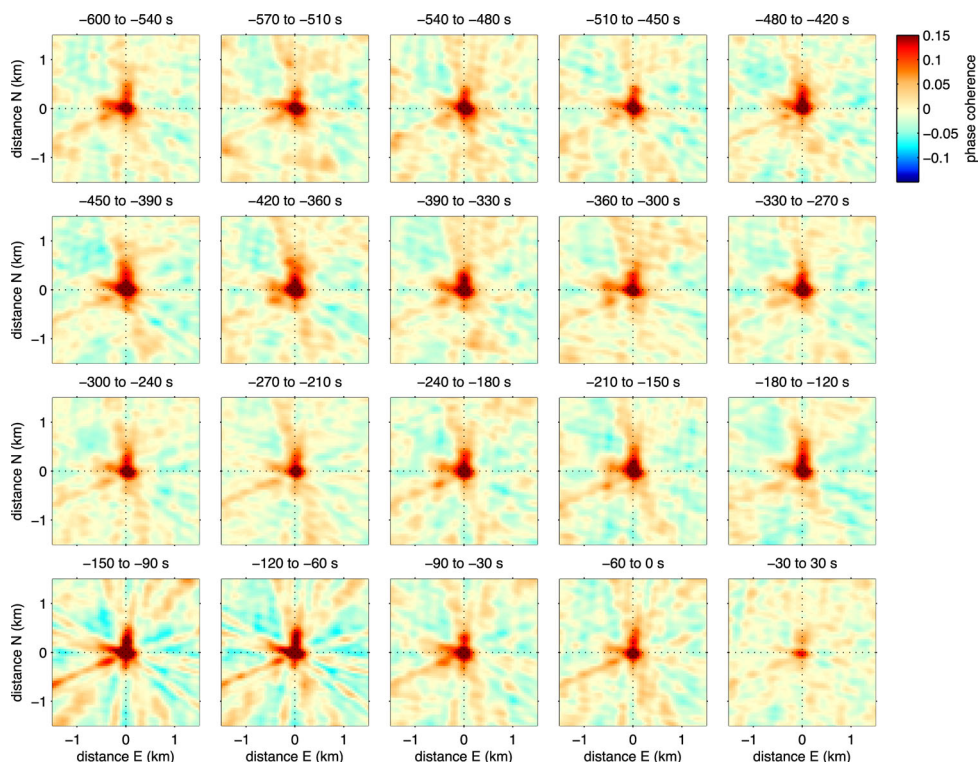

Figure 14. Phase coherence as a function of the proposed tremor location relative to the earthquake, calculated in 60 s windows indicated by the titles. For each location we time shift the seismograms to match the expected change in traveltime and recompute the coherence. The high coherence near the origin is consistent with the tremor and earthquakes being co-located. These horizontal slices are taken with no vertical offset from the earthquake location.

especially useful in the two examples here, where we compare impulsive earthquakes with tremor-like signals. The method is effectively a modification of empirical matched field analysis (e.g. Harris & Kvaerna 2010; Wang *et al.* 2015), but our implementation allows for resolution of the tremor sources on timescales shorter than the Green's function template, down to the Green's function autocorrelation time. Our phase coherence analysis of the precursory seismic signal of the 2012 April 11 *M* 3.9 Nenana, AK earthquake shows that the foreshocks are located within 2 km of the mainshock. They may have been triggered by aseismic slip associated with the mainshock nucleation. The phase coherence analysis of the tremor preceding the 2009 March 27 eruption of Redoubt Volcano confirms that the tremor is composed of repeating earthquakes located within 0.5 km of the earthquakes that preceded the tremor, and thus facilitates a more confident analysis of the tremor's properties. The high phase coherence remains significant at the 70 per cent level up until the time of the eruption, suggesting that tremor may persist even though the seismic amplitude decreases in the last 30 s. The phase coherence technique introduced here is thus a useful tool for identifying and analysing long-duration seismic signals.

ACKNOWLEDGEMENTS

REFERENCES

Ampuero, J.-P. & Rubin, A.M., 2008. Earthquake nucleation on rate and state faults — aging and slip laws, *J. geophys. Res.,* **113,** B01302, doi:10.1029/2007JB005082.

Ampuero, J.-P., Vilotte, J.-P. & Sánchez-Sesma, F.J., 2002. Nucleation of rupture under slip dependent friction law: simple models of fault zone, *J. geophys. Res.,* **107**(B12), 2324, doi:10.1029/2001JB000452.

Ando, R., Takeda, N. & Yamashita, T., 2012. Propagation dynamics of seismic and aseismic slip governed by fault heterogeneity and Newtonian rheology, *J. geophys. Res.,* **117,** B11308, doi:10.1029/2012JB009532.

Armbruster, J.G., Kim, W.-Y. & Rubin, A.M., 2014. Accurate tremor locations from coherent S and P waves, *J. geophys. Res.,* **119**(6), 5000–5013.

Baggeroer, A., Kuperman, W. & Mikhalevsky, P., 1993. An overview of matched field methods in ocean acoustics, *IEEE J. Ocean. Eng.,* **18**(4), 401–424.

Baggeroer, A.B., Kuperman, W.A. & Schmidt, H., 1988. Matched field processing: source localization in correlated noise as an optimum parameter estimation problem, *J. acoust. Soc. Am.,* **83**(2), 571–587.

Beaudoin, B.C., Fuis, G.S., Mooney, W.D., Nokleberg, W.J. & Christensen, N.I., 1992. Thin, low-velocity crust beneath the southern Yukon-Tanana Terrane, east central Alaska: Results from Trans-Alaska crustal transect refraction/wide-angle reflection data, *J. geophys. Res.,* **97**(B2), 1921–1942.

Bendat, J.S. & Piersol, A.G., 2010. *Random Data: Analysis and Measurement Procedures,* 4th edn, Wiley.

Beroza, G.C. & Ellsworth, W.L., 1996. Properties of the seismic nucleation phase, *Tectonophysics,* **261**(1–3), 209–227.

Bostock, M.G., Royer, A.A., Hearn, E.H. & Peacock, S.M., 2012. Low frequency earthquakes below southern Vancouver Island, *Geochem. Geophys. Geosyst.,* **13,** Q11007, doi:10.1029/2012GC004391.

Bouchon, M., Karabulut, H., Aktar, M., Özalaybey, S., Schmittbuhl, J. & Bouin, M.-P., 2011. Extended nucleation of the 1999 Mw 7.6 Izmit earthquake, *Science,* **331**(6019), 877 –880.

Bouchon, M., Durand, V., Marsan, D., Karabulut, H. & Schmittbuhl, J., 2013. The long precursory phase of most large interplate earthquakes, *Nat. Geosci.,* **6**(4), 299–302.

Brodsky, E.E. & van der Elst, N.J., 2010. Connecting near-field and far-field earthquake triggering to dynamic strain, *J. geophys. Res.,* **115,** B07311, doi:10.1029/2009JB006681.

Brown, J.R. *et al.,* 2009. Deep low-frequency earthquakes in tremor localize to the plate interface in multiple subduction zones, *Geophys. Res. Lett.,* **36,** L19306, doi:10.1029/2009GL040027.

Bucker, H.P., 1976. Use of calculated sound fields and matched-field detection to locate sound sources in shallow water, *J. acoust. Soc. Am.,* **59**(2), 368–373.

Buurman, H., West, M.E. & Thompson, G., 2013. The seismicity of the 2009 Redoubt eruption, *J. Volcanol. Geotherm. Res.,* **259,** 16–30.

Campillo, M. & Ionescu, I.R., 1997. Initiation of antiplane shear instability under slip dependent friction, *J. geophys. Res.,* **102**(B9), 20 363–20 371.

Chen, X. & Shearer, P.M., 2013. California foreshock sequences suggest aseismic triggering process, *Geophys. Res. Lett.,* **40**(11), 2602–2607.

Colombelli, S., Zollo, A., Festa, G. & Picozzi, M., 2014. Evidence for a difference in rupture initiation between small and large earthquakes, *Nat. Comm.,* **5,** 3958, doi:10.1038/ncomms4958.

Corciulo, M., Roux, P., Campillo, M., Dubucq, D. & Kuperman, W., 2012. Multiscale matched-field processing for noise-source localization in exploration geophysics, *Geophysics,* **77**(5), KS33–KS41.

Cros, E., Roux, P., Vandemeulebrouck, J. & Kedar, S., 2011. Locating hydrothermal acoustic sources at Old Faithful Geyser using matched field processing, *Geophys. J. Int.,* **187**(1), 385–393.

Crotwell, H.P., Owens, T.J. & Ritsema, J., 1999. The TauP toolkit: flexible seismic travel-time and ray-path utilities, *Seismol. Res. Lett.,* **70**(2), 154–160.

Dieterich, J.H., 1992. Earthquake nucleation on faults with rate-dependent and state-dependent strength, *Tectonophysics,* **211**(1–4), 115–134.

Dixon, J.P., Stihler, S.D., Power, J.A. & Searcy, C., 2010. Catalog of earthquake hypocenters at Alaskan volcanoes: January 1 through December 31, 2009, Tech. Rep. 531, USGS.

Dmitrieva, K., Hotovec-Ellis, A.J., Prejean, S. & Dunham, E.M., 2013. Frictional-faulting model for harmonic tremor before Redoubt Volcano eruptions, *Nat. Geosci.,* **6**(8), 652–656.

Dodge, D.A., Beroza, G.C. & Ellsworth, W.L., 1996. Detailed observations of California foreshock sequences: implications for the earthquake initiation process, *J. geophys. Res.,* **101**(B10), 22 371–22 392.

Ellsworth, W.L. & Beroza, G.C., 1995. Seismic evidence for an earthquake nucleation phase, *Science,* **268**(5212), 851–855.

Fang, Z., Dieterich, J.H., Richards-Dinger, K.B. & Xu, G., 2011. Earthquake nucleation on faults with nonconstant normal stress, *J. geophys. Res.,* **116,** B09307, doi:10.1029/2011JB008196.

Fehler, M., 1983. Observations of volcanic tremor at Mount St. Helens Volcano, *J. geophys. Res.,* **88**(B4), 3476–3484.

Fialkowski, L.T., Collins, M.D., Kuperman, W.A., Perkins, J.S., Kelly, L.J., Larsson, A., Fawcett, J.A. & Hall, L.H., 2000. Matched-field processing using measured replica fields, *J. acoust. Soc. Am.,* **107**(2), 739–746.

Garagash, D.I. & Germanovich, L.N., 2012. Nucleation and arrest of dynamic slip on a pressurized fault, *J. geophys. Res.,* **117,** B10310, doi:10.1029/2012JB009209.

Gibbons, S.J. & Ringdal, F., 2009. Detection and analysis of near-surface explosions on the Kola Peninsula, *Pure appl. Geophys.,* **167**(4–5), 413–436.

Gomberg, J. & Davis, S., 1996. Stress/strain changes and triggered seismicity at the Geysers, California, *J. geophys. Res.,* **101,** 733–750.

Gomberg, J., Agnew, D.C. & Schwartz, S.Y., 2016. Alternative source models of very low frequency events, *J. geophys. Res.,* **121**(9), 6722–6740.

Harrington, R.M. & Brodsky, E.E., 2007. Volcanic hybrid earthquakes that are brittle-failure events, *Geophys. Res. Lett.,* **34,** L06308, doi:10.1029/2006GL028714.

Harris, F.J., 1978. Use of windows for harmonic analysis with discrete Fourier transform, *Proc. IEEE,* **66**(1), 51–83.

Harris, D.B. & Kvaerna, T., 2010. Superresolution with seismic arrays using empirical matched field processing, *Geophys. J. Int.,* **182**(3), 1455–1477.

Hill, D.P. & Prejean, S.G., 2007. Dynamic triggering, in *Treatise on Geophysics, Earthquake Seismology*, vol. 4, p. 6054, eds   Kanamori, H. & Schubert, G., Elsevier.

Hill, D.P. *et al.*, 1993. Seismicity remotely triggered by the magnitude 7.3 Landers, California, earthquake, *Science,* **260,** 1617–1623.

Hotovec, A.J., Prejean, S.G., Vidale, J.E. & Gomberg, J., 2013. Strongly gliding harmonic tremor during the 2009 eruption of Redoubt Volcano, *J. Volcanol. Geotherm. Res.,* **259,** 89–99.

Ide, S., Shelly, D.R. & Beroza, G.C., 2007. Mechanism of deep low frequency earthquakes: further evidence that deep non-volcanic tremor is generated by shear slip on the plate interface, *Geophys. Res. Lett.,* **34**(3), L03308, doi:10.1029/2006GL028890.

Ishii, M., Shearer, P.M., Houston, H. & Vidale, J.E., 2007. Teleseismic P wave imaging of the 26 December 2004 Sumatra-Andaman and 28 March 2005 Sumatra earthquake ruptures using the Hi-net array, *J. geophys. Res.,* **112,** B11307, doi:10.1029/2006JB004700.

Iverson, R.M. *et al.*, 2006. Dynamics of seismogenic volcanic extrusion at Mount St Helens in 2004–05, *Nature,* **444**(7118), 439–443.

Johnston, M.J.S., Borcherdt, R.D., Linde, A.T. & Gladwin, M.T., 2006. Continuous borehole strain and pore pressure in the near field of the 28 September 2004 M 6.0 Parkfield, California, earthquake: implications for nucleation, fault response, earthquake prediction, and tremor, *Bull. seism. Soc. Am.,* **96**(4B), S56–S72.

Kato, A., Obara, K., Igarashi, T., Tsuruoka, H., Nakagawa, S. & Hirata, N., 2012. Propagation of slow slip leading up to the 2011 Mw 9.0 Tohoku-Oki earthquake, *Science,* **335**(6069), 705 –708.

Koehler, R.D., Farrell, R.-E., Burns, P.A.C. & Combellick, R.A., 2012. *Quaternary Faults and Folds in Alaska: A Digital Database,* Alaska Division of Geological & Geophysical Surveys, p. 141.

Krolik, J.L., 1992. Matched-field minimum variance beamforming in a random ocean channel, *J. acoust. Soc. Am.,* **92**(3), 1408–1419.

Lahr, J.C., Chouet, B.A., Stephens, C.D., Power, J.A. & Page, R.A., 1994. Earthquake classification, location, and error analysis in a volcanic environment: implications for the magmatic system of the 1989–1990 eruptions at redoubt volcano, Alaska, *J. Volcanol. Geotherm. Res.,* **62**(1–4), 137–151.

Lapusta, N. & Rice, J.R., 2003. Nucleation and early seismic propagation of small and large events in a crustal earthquake model, *J. geophys. Res.,* **108**(B4), 2205, doi:10.1029/2001JB000793.

Latour, S., Schubnel, A., Nielsen, S., Madariaga, R. & Vinciguerra, S., 2013. Characterization of nucleation during laboratory earthquakes, *Geophys. Res. Lett.,* **40**(19), 5064–5069.

Lindseth, R.O., 1968. Vibroseis, in *Digital Processing of Geophysical Data—A Review*, pp. 7.1–7.14, Society of Exploration Geophysicists.

McLaskey, G.C. & Kilgore, B.D., 2013. Foreshocks during the nucleation of stick-slip instability, *J. geophys. Res.,* **118**(6), 2982–2997.

McLaskey, G.C. & Lockner, D.A., 2014. Preslip and cascade processes initiating laboratory stick slip, *J. geophys. Res.,* **119**(8), 6323–6336.

Meng, L., Inbal, A. & Ampuero, J.-P., 2011. A window into the complexity of the dynamic rupture of the 2011 Mw 9 Tohoku-Oki earthquake, *Geophys. Res. Lett.,* **38,** L00G07, doi:10.1029/2011GL048118.

Mori, J. & Frankel, A., 1990. Source parameters for small events associated with the 1986 North Palm Springs, California, earthquake determined using empirical Green functions, *Bull. seism. Soc. Am.,* **80**(2), 278–295.

Mueller, C.S., 1985. Source pulse enhancement by deconvolution of an empirical Green's function, *Geophys. Res. Lett.,* **12**(1), 33–36.

Nadeau, R.M. & McEvilly, T.V., 1999. Fault slip rates at depth from recurrence intervals of repeating microearthquakes, *Science,* **285**(5428), 718–721.

Neuberg, J., Luckett, R., Baptie, B. & Olsen, K., 2000. Models of tremor and low-frequency earthquake swarms on Montserrat, *J. Volcanol. Geotherm. Res.,* **101**(1–2), 83–104.

Neuberg, J.W., Tuffen, H., Collier, L., Green, D., Powell, T. & Dingwell, D., 2006. The trigger mechanism of low-frequency earthquakes on Montserrat, *J. Volcanol. Geotherm. Res.,* **153**(1–2), 37–50.

Noda, H., Nakatani, M. & Hori, T., 2013a. Large nucleation before large earthquakes is sometimes skipped due to cascade-up—implications from a rate and state simulation of faults with hierarchical asperities, *J. geophys. Res.,* **118**(6), 2924–2952.

Noda, H., Nakatani, M. & Hori, T., 2013b. A slower fault may produce a smaller preseismic moment rate: Non-1/t_f acceleration of moment rate during nucleation and dependency on the background slip rate, *Geophys. Res. Lett.,* **40**(18), 4850–4854.

Ohnaka, M., 1992. Earthquake source nucleation: a physical model for short-term precursors, *Tectonophysics,* **211,** 149–178.

Ohnaka, M., 2000. A physical scaling relation between the size of an earthquake and its nucleation zone size, *Pure appl. Geophys.,* **157,** 2259–2282.

Ohnaka, M. & Shen, L.-F., 1999. Scaling of the shear rupture process from nucleation to dynamic propagation: implications of geometric irregularity of the rupturing surfaces, *J. geophys. Res.,* **104,** 817–844.

Peng, Y., Rubin, A.M., Bostock, M.G. & Armbruster, J.G., 2015. High-resolution imaging of rapid tremor migrations beneath southern Vancouver Island using cross-station cross correlations, *J. geophys. Res.,* **120**(6), 4317–4332.

Peng, Z. & Zhao, P., 2009. Migration of early aftershocks following the 2004 Parkfield earthquake, *Nat. Geosci.,* **2**(12), 877–881.

Percival, D.B. & Walden, A.T., 1993. *Spectral Analysis for Physical Applications,* 1st edn, Cambridge Univ. Press.

Powell, T.W. & Neuberg, J., 2003. Time dependent features in tremor spectra, *J. Volcanol. Geotherm. Res.,* **128**(1–3), 177–185.

Ratchkovski, N.A. & Hansen, R.A., 2002. New constraints on tectonics of interior Alaska: earthquake locations, source mechanisms, and stress regime, *Bull. seism. Soc. Am.,* **92**(3), 998–1014.

Richards-Dinger, K., Stein, R.S. & Toda, S., 2010. Decay of aftershock density with distance does not indicate triggering by dynamic stress, *Nature,* **467**(7315), 583–586.

Ripperger, J., Ampuero, J.-P., Mai, P.M. & Giardini, D., 2007. Earthquake source characteristics from dynamic rupture with constrained stochastic fault stress, *J. geophys. Res.,* **112,** B04311, doi:10.1029/2006JB004515.

Rubin, A.M. & Ampuero, J.P., 2005. Earthquake nucleation on (aging) rate and state faults, *J. geophys. Res.,* **110,** B11312, doi:10.1029/2005JB003686.

Rubin, A.M. & Armbruster, J.G., 2013. Imaging slow slip fronts in Cascadia with high precision cross-station tremor locations, *Geochem. Geophys. Geosyst.,* **14,** 5371–5392.

Rubinstein, S.M., Cohen, G. & Fineberg, J., 2009. Visualizing stick–slip: experimental observations of processes governing the nucleation of frictional sliding, *J. Phys. D: Appl. Phys.,* **42,** 214016, doi:10.1088/0022-3727/42/21/214016.

Rydelek, P.A. & Hass, L., 1994. On estimating the amount of blasts in seismic catalogs with Schuster's method, *Bull. seism. Soc. Am.,* **84**(4), 1256–1259.

Savard, G. & Bostock, M.G., 2015. Detection and location of low-frequency earthquakes using cross-station correlation, *Bull. seism. Soc. Am.,* **105**(4), 2128–2142.

Schuster, A., 1897. On lunar and solar periodicies of earthquakes, *Proc. R. Soc. A,* **61**(369–377), 455–465.

Shearer, P.M., 2012. Self-similar earthquake triggering, Bath's law, and foreshock/aftershock magnitudes: simulations, theory, and results for southern California, *J. geophys. Res.,* **117,** B06310, doi:10.1029/2011JB008957.

Shelly, D.R., Beroza, G.C. & Ide, S., 2007. Non-volcanic tremor and low-frequency earthquake swarms, *Nature,* **446**(7133), 305–307.

Slepian, D., 1976. On bandwidth, *Proc. IEEE,* **64**(3), 292–300.

Sweet, J.R., Creager, K.C. & Houston, H., 2014. A family of repeating low-frequency earthquakes at the downdip edge of tremor and slip, *Geochem. Geophys. Geosyst.,* **15**(9), 3713–3721.

Tanaka, S., Ohtake, M. & Sato, H., 2002. Evidence for tidal triggering of earthquakes as revealed from statistical analysis of global data, *J. geophys. Res.,* **107**(B10), 2211, doi:10.1029/2001JB001577.

Tape, C., West, M., Silwal, V. & Ruppert, N., 2013. Earthquake nucleation and triggering on an optimally oriented fault, *Earth planet. Sci. Lett.,* **363,** 231–241.

Thomson, D.J., 1982. Spectrum estimation and harmonic analysis, *Proc. IEEE,* **70**(9), 1055–1096.

Tyapkin, Y. & Ursin, B., 2005. Optimum stacking of seismic records with irregular noise, *J. Geophys. Eng.,* **2**(3), 177–187.

USGS, 2015. *USGS NED 2 arc-second DEM ArcGrid 2015*, Tech. rep., Reston, VA.

Velasco, A.A., Ammon, C.J. & Lay, T., 1994. Empirical green function deconvolution of broadband surface waves: rupture directivity of the 1992 Landers, California (M_w = 7.3), earthquake, *Bull. seism. Soc. Am.,* **84**(3), 735–750.

Waldhauser, F. & Schaff, D.P., 2008. Large-scale relocation of two decades of Northern California seismicity using cross-correlation and double-difference methods, *J. geophys. Res.,* **113,** B08311, doi:10.1029/2007JB005479.

Wang, J., Templeton, D.C. & Harris, D.B., 2015. Discovering new events beyond the catalogue—application of empirical matched field processing to Salton Sea geothermal field seismicity, *Geophys. J. Int.,* **203**(1), 22–32.

Yagi, Y., Nakao, A. & Kasahara, A., 2012. Smooth and rapid slip near the Japan Trench during the 2011 Tohoku-oki earthquake revealed by a hybrid back-projection method, *Earth planet. Sci. Lett.,* **355–356,** 94–101.

SUPPORTING INFORMATION

Supplementary data are available at *GJIRAS* online.

Figure S1. Red curves: distribution of phase coherence values between an earthquake and noisy seismograms. Yellow curves: distribution obtained by generating random complex numbers to represent the Fourier coefficients and computing their phase coherence. Blue curves: normal distributions. Dashed purple curves: analytical distribution expected from averaging values taken from an exponential distribution (equation (S19)), expected to be a good approximation when a large number of station pairs N_p are included. The standard deviations of the observed and synthetic phase coherence values are well matched by $\sqrt{2N_f N_t N_p}$. The first column, panels a–c, shows the effect of averaging over frequencies. Individual coherence values (panel a) follow a cosine distribution, while their averages (panels b and c) converge toward a normal distribution. The second column, panels d–f, shows the effect of averaging with multiple tapers. Columns 1 and 2 use only one station. The final column, panels g–i, shows the effect of averaging over station pairs. The averaging reduces the noise, but the distributions have tails at positive values because the values being averaged are not all independent. Once at least 5 or so stations are included, the observed distributions tend toward the distribution modeled with equation (S19).

Figure S2. Fraction of values in the distributions that exceed 1 (red), 2 (yellow), 3 (green), or 4σ (blue). The horizontal lines indicate the fraction expected for normal distributions. The symbols are the fractions obtained from coherence values with the specified numbers of station pairs and frequencies. The standard deviation is assumed to be $1/\sqrt{2N_f N_p}$, and this is a good match of the 1σ estimate. However, more of the phase coherence values exceed 2, 3, and 4σ than would be expected for normal distributions

Figure S3. (a,d,g) Blue: numerical distributions of the moveout amplitudes s after summing randomly oriented vectors with length 1. The number of stations N_s is indicated at the top of each column. Red: expected distribution of values from equation (S15). (b,e,h) Numerical (blue) and expected (red, equation (S18)) distributions of phase coherence after averaging over station pairs. (c,f,h) Numerical (blue) and expected (red, equation (S19)) distributions of phase coherence after averaging over station pairs and over 10 independent frequencies.

Figure S4. Phase coherence of synthetic data with various source and window lengths. In (a), the source duration is 0.1 seconds and the window lengths are as indicated by the horizontal bars: 0.5, 1, 3, or 5 seconds. In (b), the window length is 0.1 seconds and the source durations are as indicated by the horizontal bars: 0.1, 1, 3, or 5 seconds. In all cases, the duration of high coherence is roughly equal to the sum of the window length and the source duration.

Figure S5. (a–m) Autocorrelation of the templates used for the Nenana observations, normalized to the maximum value. (n–z) Fraction of the energy in the cross-correlation that is within the specified time of zero.

Figure S6. (a–e) Autocorrelation of the templates used for the Redoubt earthquakes, normalized to the maximum value. (f–j) Fraction of the energy in the cross-correlation that is within the specified time of zero.

Figure S7. East-striking vertical cross-section of the phase coherence between the precursor and earthquake. This slice is taken with no offset in the N–S direction. For each location, the template seismograms are shifted according to the change in *P* wave travel time, and the phase coherence is recomputed.

Figure S8. North-striking vertical cross-section of the phase coherence between the precursor and earthquake. This slice is taken with no offset in the E–W direction. For each location, the template seismograms are shifted according to the change in *P* wave travel time, and the phase coherence is recomputed.

Figure S9. Horizontal cross-section of the synthetic signal coherence. This slice is taken with no offset in the N–S direction. For each location, the template seismograms are shifted according to the change in *P* wave travel time, and the phase coherence is recomputed.

Figure S10. East-striking vertical cross-section of the phase coherence between the synthetic signal and earthquake.

Figure S11. North-striking vertical cross-section of the phase coherence between the synthetic signal and earthquake.

Figure S12. East-striking vertical cross-section of the phase coherence between the volcanic tremor and repeating earthquake template. This slice is taken with no offset in the N–S direction.

Figure S13. North-striking vertical cross-section of the phase coherence between the volcanic tremor and repeating earthquake template. This slice is taken with no offset in the E–W direction.

Figure S14. Horizontal cross-section of the phase coherence between the volcanic tremor and repeating earthquake template, as in Fig. 14, but with a shorter, 2-second-long template that is more dominated by the *P* wave arrival. We compute the time shifts according to *P*-wave velocities. The spatial of high phase coherence is similar to that estimated with the longer template more dominated by the *S* wave, though the magnitude of the coherence is lower with this truncated template.